



Supporting Information

Iterative Arylation of Amino Acids and Aliphatic Amines via δ -C(sp³)–H Activation: Experimental and Computational Exploration

Srimanta Guin⁺, Pravas Dolui⁺, Xinglong Zhang, Satyadip Paul, Vikas Kumar Singh, Sukumar Pradhan, Hediyala B. Chandrashekar, S. S. Anjana, Robert S. Paton, and Debabrata Maiti**

anie_201900479_sm_miscellaneous_information.pdf

Computational Part, Part 2

Contents

I. Computational Methods	S201
II. Computational study of <i>N</i>-(2,4,4-trimethylpentan-2-yl)picolinamide (substrate 2a)	S202
II.1 Reaction pathway involving mononuclear Pd(II) catalyst	S202
II.2 Stable polynuclear complexes of Palladium catalyst	S205
II.3 Trinuclear pathway for Pd(II) catalysis – first arylation	S206
II.4 Second and third arylation	S209
II.5 Effects of directing groups	S214
III. Computational study of <i>N</i>-(4-methylpentan-2-yl)picolinamide (substrate 3a)	S220
III.1 Reaction pathway involving mononuclear Pd(II) catalyst	S220
III.2 Reaction pathway involving trinuclear Pd(II) catalyst	S221
III.3 Reaction pathway involving silver carbonate as co-ligand	S224
III.4 C–H activation step	S226
III.5 Isodesmic formations of C–H activation step	S228
IV. Regioselectivity studies	S228
IV.1 Regioselectivity in <i>N</i>-(4-methylhexan-2-yl)picolinamide (substrate 4a)	S228
IV.2 Regioselectivity study in 3,5,5-trimethylcyclohexanamine (substrate 5a)	S230
IV.3 Regioselectivity study in 3-methylcyclohexanamine (substrate 6a)	S231
IV.4 Regioselectivity study in 3-pinanamine (substrate 7a)	S232
V. Absolute values for optimised structures	S234
VI. References	S240

I. Computational Methods

Density functional theory (DFT) calculations were performed with *Gaussian 16* rev. A.03.¹ Geometry optimisations were carried out using global-hybrid meta-NGA (nonseparable gradient approximation) MN15 functional² with a mixed Karlsruhe-family basis set of triple- ζ valence def2-TZVPPD (where ‘D’ indicates diffuse basis functions) for Pd³, Ag⁴ and I⁵ atoms and def2-SVP^{6,7} for all other atoms (BS1). This recently developed functional was chosen as it performs much better than many other functionals in predicting transition metal reaction barrier heights.² Previously, Pd(II)-catalysed C-C bond formations have been studied using other functionals including meta-GGA TPSS and range-separated ω B97X-D functionals.^{8,9} MN15 has been shown to give better agreement in geometry predictions of both transition metal complex and organic molecules² and in reproducing the energetic profile of trinuclear Cu-catalysed methane-to-methanol catalytic conversion¹⁰ than many other functionals including ω B97X-D and TPSS. Minima and transition structures on the potential energy surface (PES) were confirmed as such by harmonic frequency analysis, showing respectively zero and one imaginary frequency, at the same level of theory. Single point (SP) corrections were performed with MN15 functional and the same basis set as before except where def2-SVP was replaced by def2-TZVPP basis set (BS2). The SMD continuum solvation model¹¹ was carried out to include the effect of *tert*-butyl methyl ether (TBME) solvent on the computed Gibbs energy profile. TBME solvent was parametrized using a set of solvent parameters. These include the static dielectric constant of the solvent at 25°C (*Eps*=2.6);¹² dynamic dielectric constant – the square of the refractive index value of 1.3664 at 20°C was used¹³ (*EpsInf*=1.867); hydrogen bond acidity (*HBondAcidity*=0.00) and basicity (*HBondBasicity*=0.54),¹⁴ which are Abraham’s *A* and *B* values respectively; surface tension at interface (*SurfaceTensionAtInterface*=15.717);¹⁵ carbon aromaticity – fraction of aromatic carbons (*CarbonAromaticity*=0.00) and electronegative halogenicity – fraction of halogens (*ElectronegativeHalogenicity*=0.00). These parameters were specified using the keyword “SCRF=(SMD, solvent=Generic, Read)” in *Gaussian 16*. Gibbs energies were evaluated at 363.15 K, using a quasi-RRHO treatment of vibrational entropies.^{16,17} Vibrational entropies of frequencies below 100 cm⁻¹ were obtained according to a free rotor description, using a smooth damping function to interpolate between the two limiting descriptions.¹⁶ The free energies were further corrected using standard concentration of 1 mol/L, which were used in solvation calculations.

Stereoelectronic properties, including donor-acceptor interactions and steric effects, were analysed using NBO¹⁸ and NCIPILOT¹⁹ calculations, respectively. The *wfn* files for NCIPILOT were generated at MN15/DGDZVP^{20,21} level of theory. Noncovalent interaction (NCI) indices calculated with NCIPILOT were visualised at gradient isosurfaces value of *s* = 0.5 au. These are coloured according to the sign of (λ_2) over the range of -0.1 (blue = attractive) to +0.1 (red = repulsive). All molecular structures and molecular orbitals were visualized using *PyMOL* software.²²

Geometries of all structures (in .xyz format with their associated energy in Hartrees) are included in a separate folder named *structures_xyz* and have been deposited with this Supporting Information.

II. Computational study of *N*-(2,4,4-trimethylpentan-2-yl)picolinamide (substrate 2a)

II.1 Reaction pathway involving mononuclear Pd(II) catalyst

The solvent-corrected energy profile for the mononuclear pathways is shown in Figure S1. The palladacycle formation occurred with two successive concerted metalation-deprotonation (CMD) steps. The initial coordination of picolinamide molecule to monomeric $\text{Pd}(\text{TFA})_2$ was assisted by the formation of hydrogen bonding between amide-H and oxygen atom on one of the trifluoroacetate (TFA) ligands. The amide N–H proton was easily deprotonated by the coordinating TFA ligand while Pd interacted with the breaking N–H nitrogen (**ts-1**). This CMD step, albeit facile, was reversible. The immediate loss of a trifluoroacetic acid (HTFA) molecule made this step exergonic, giving **int-3** at 1.1 kcal mol⁻¹. In the absence of pyridine ligand, one of the coordination sites on Pd got displaced by C–H bond, which coordinated to the Pd metal by agostic interaction. The non-coordinating O atom of the TFA ligand then carried out a second CMD (**ts-4'**), forming Pd–C bond in intermediate **int-5'**. This CMD step was reversible. The TSs for oxidative addition (OA) (**ts-6**) of aryliodide and reductive elimination (RE) (**ts-7**) of C–C bond formation had comparable Gibbs energy of activation. The first arylation product, **int-8**, at -8.1 kcal mol⁻¹, was thermodynamically stable with respect to the starting material or any prior intermediates, making the reaction favourable under thermodynamic control. Different conformations of each TSs were considered, in particular, we found that the 6-membered palladacycle could adopt two conformations (Figure S2), with the ring puckered in opposite orientations. The lowest energy conformations were taken for discussion in the main text, assuming that the conformers can interconvert easily and rapidly.

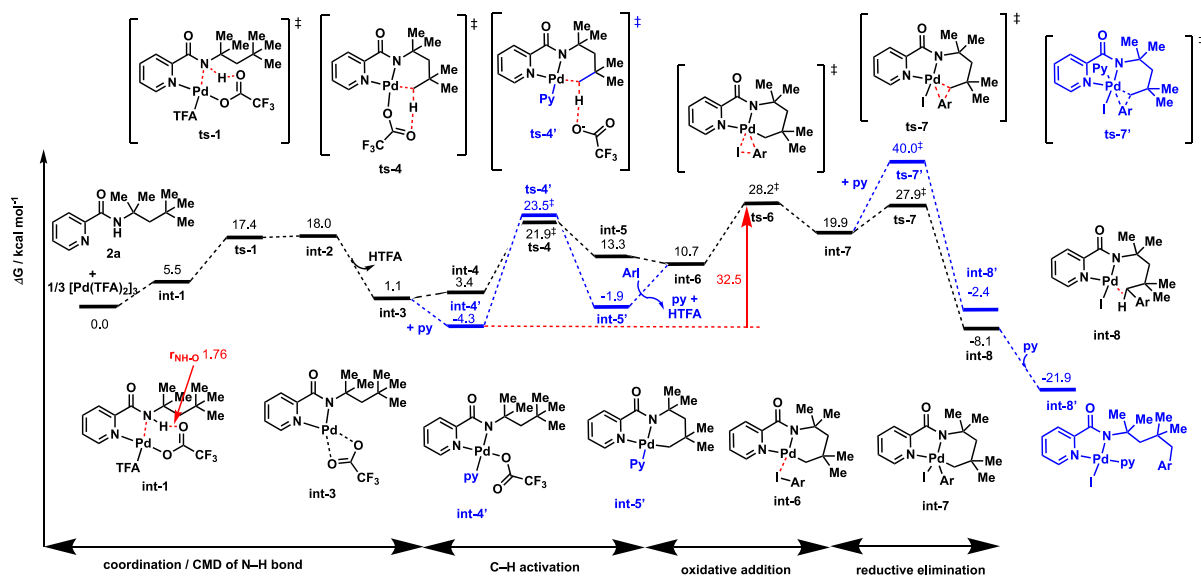
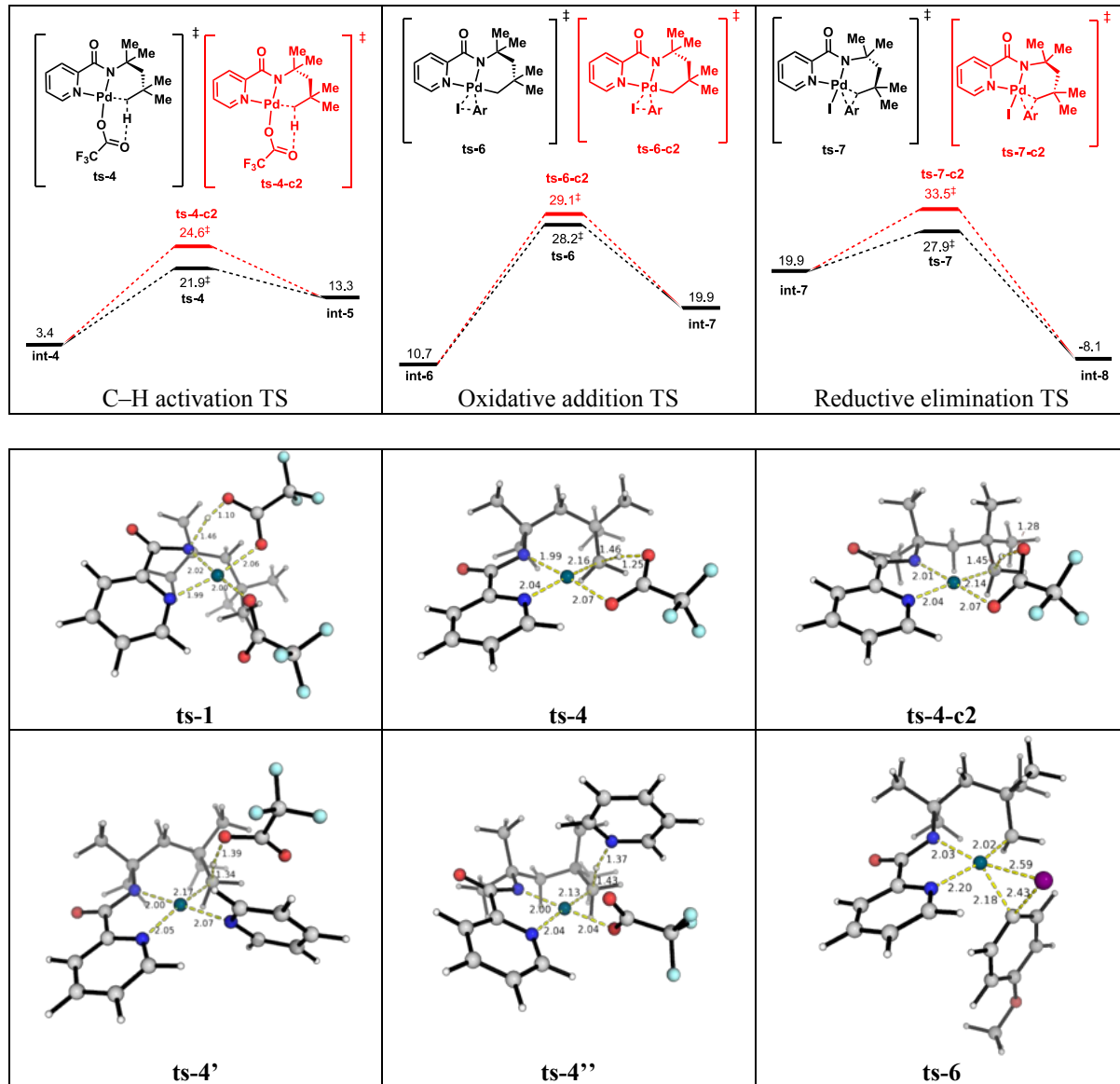


Figure S1. Gibbs free energy profile for first arylation in the absence (black) and presence (blue) of pyridine ligand as computed by SMD(TBME)-MN15/BS2//MN15/BS1. All values are quoted in kcal mol⁻¹.

In the presence of pyridine, we found no TSs that were lowered in activation barrier by direct pyridine participation. In particular, pyridine molecule could not coordinate to Pd metal during OA of aryl iodide. The displacement of pyridyl group on the picolinamide by pyridine was also unfavourable. For RE, although pyridine could coordinate to Pd, this TS (ts-7') however, had a much higher activation barrier (by 12.1 kcal mol⁻¹) than that without pyridine



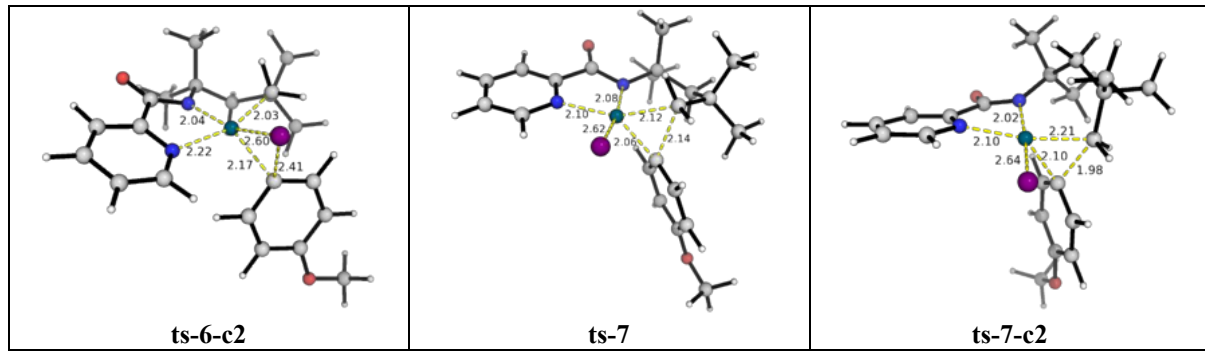
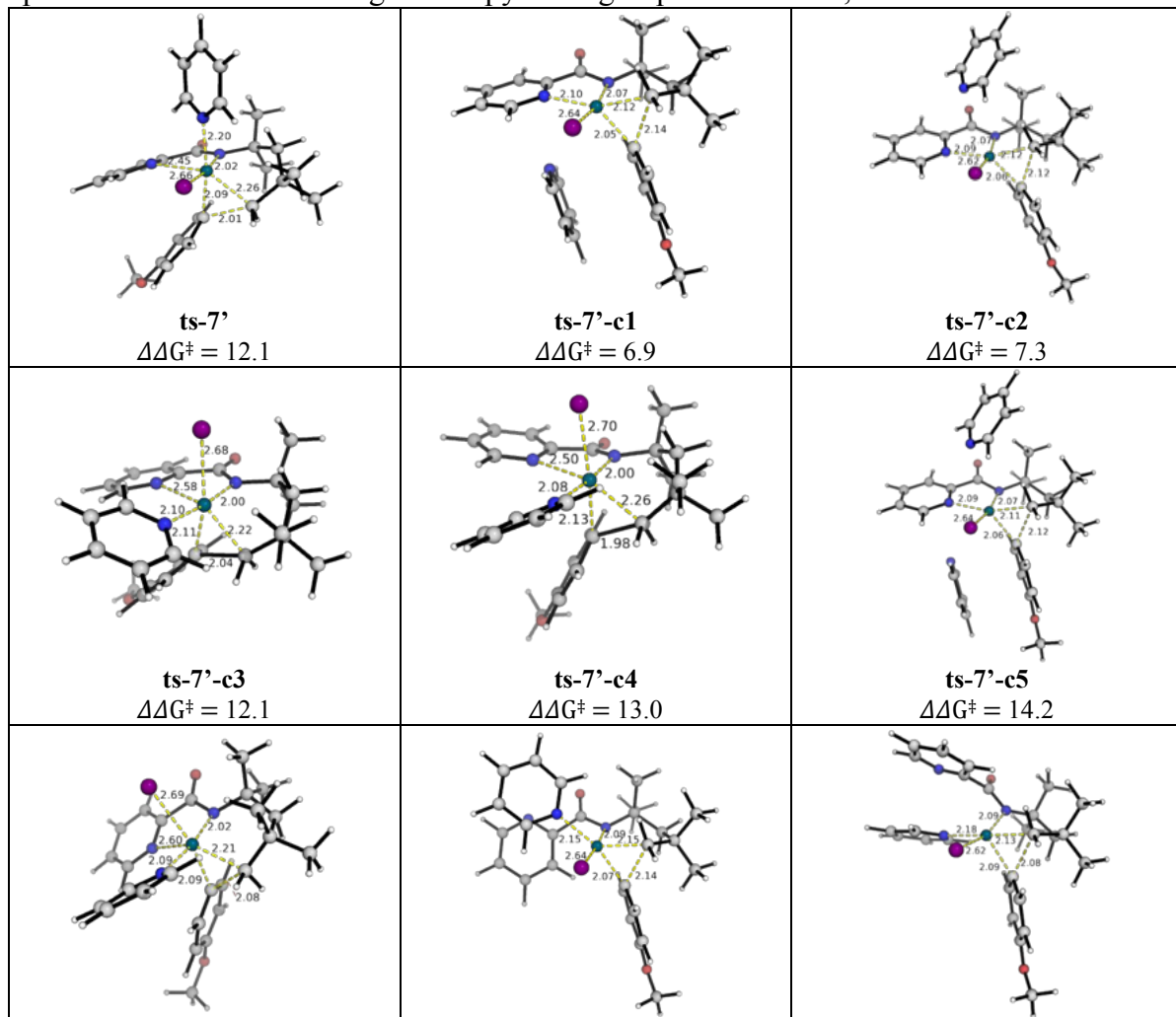


Figure S2. Top: Computed energy profiles for C–H activation, oxidative addition and reductive elimination TSs with different conformations of the 6-membered palladacycle. Bottom: Selected TS structures for the energy profile in Figure S1. Key bond distances are given in Å.

ligand (**ts-7**). A RE step with non-coordinating pyridine, **ts-7'-c1**, at 34.8 kcal mol⁻¹, however, was found to be lower in activation barrier than **ts-7'**, but still higher than without any pyridine ligand **ts-7**. This was due to the unfavourable loss of entropy as one additional molecule of pyridine was brought close to the TS. Considering the geometric isomers by swapping the positions of the coordinating I-/Ar-/pyridine groups on Pd metal, we did not



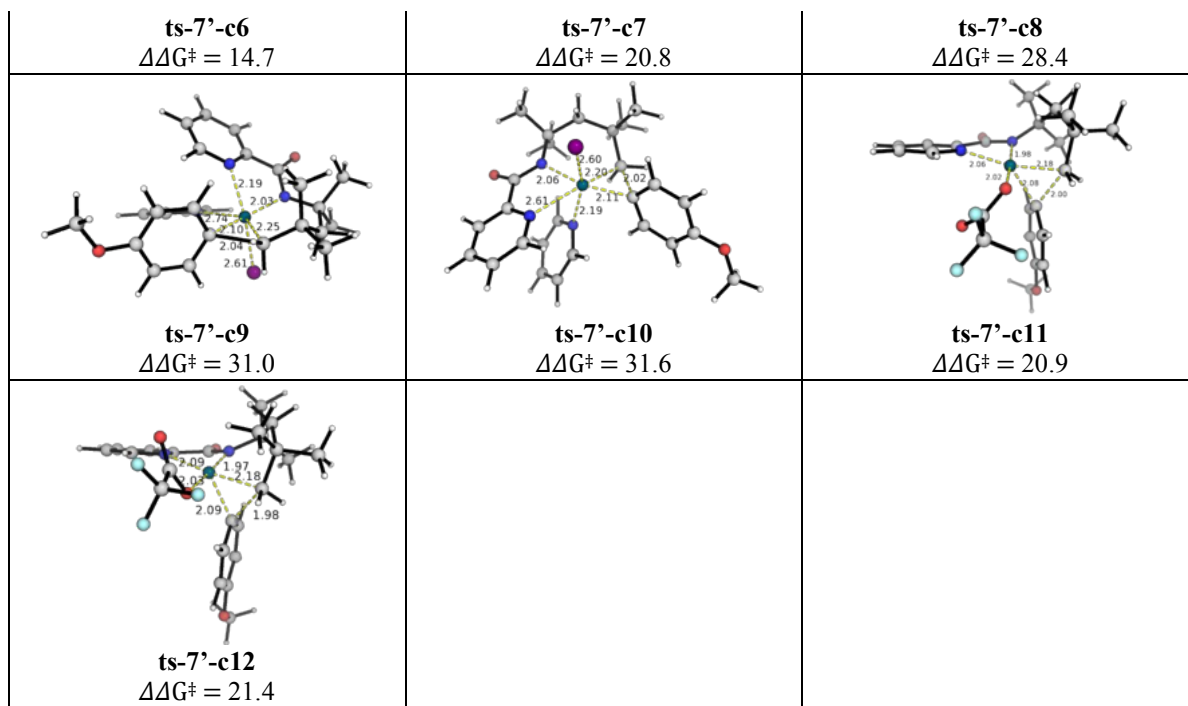


Figure S3. Transition structures considered for reductive elimination step in the presence of pyridine ligand. Gibbs free energies of activation relative to the lowest TS **ts-7** ($\Delta\Delta G^\ddagger$) are given in kcal mol⁻¹. Key bond distances are given in Å.

find any TS with lower activation barrier than that without any pyridine ligand (Figure S3). This is consistent with the observation that complexes with even number of coordination undergo RE less readily than those with odd number of coordination.²³ We also explored the possibility of ligand exchange of CF_3COO^- for I^- before reductive elimination (**ts-7'-c11** and **ts-7'-c12**) and these also had higher activation barriers than **ts-7**. Our thorough TS searches concluded that pyridine ligand did not participate directly in the reaction r.d.s. for our system.

II.2 Stable polynuclear complexes of Palladium catalyst

Palladium(II) acetate and its variants have long been known to exist in polynuclear form in both the solid state as well as in solution.^{24–26} Palladium(II) trifluoroacetate has been shown to exist in trimeric form $\text{Pd}_3(\text{TFA})_6$ in solid phase. Factors such as solvent and ligand effects influencing the trimeric/monomeric equilibrium have been explored.^{27–30} Our calculations found that the formation of dimeric complex is exergonic by -26.4 kcal mol⁻¹ and that of trimeric complex is exergonic by -56.7 kcal mol⁻¹ in TBME solvent relative to the monomeric complex, $\text{Pd}(\text{TFA})_2$. These values were in good agreement with the experimental and theoretical values for the palladium acetate system (-34.9 kcal mol⁻¹ for dimer and -59.3 kcal mol⁻¹ for trimer).^{25,30} We found that each Pd(II) atom is in a square planar environment and altogether the trimer exists in a cyclic form (Figure S4 (c)), with interactions between the paddlewheel ligands and between Pd-Pd metal centres. The most stable starting complex of palladium trifluoroacetate catalyst used in this reaction existed in trinuclear form. The consideration of a potentially polynuclear Pd-catalyst is thus necessary. More directly, the synthesis of C–H activated trinuclear complex, coupled with

computational studies, by Yu *et. al* provided unequivocal evidence for the involvement of trinuclear catalytic species in such reactions.³¹

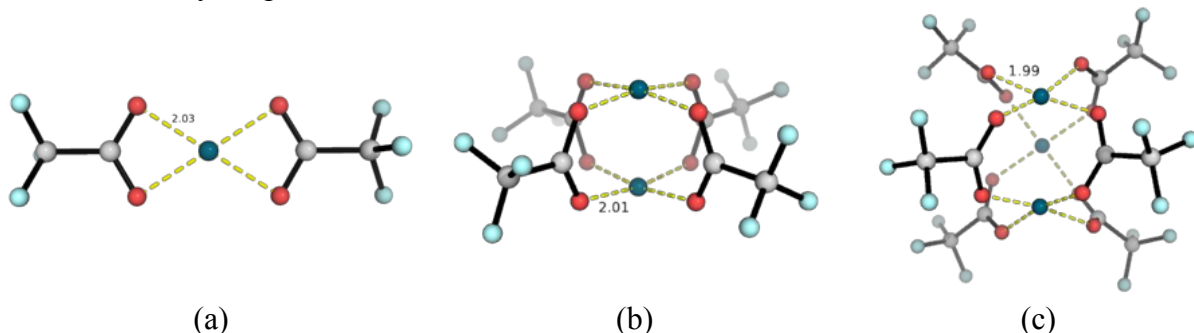
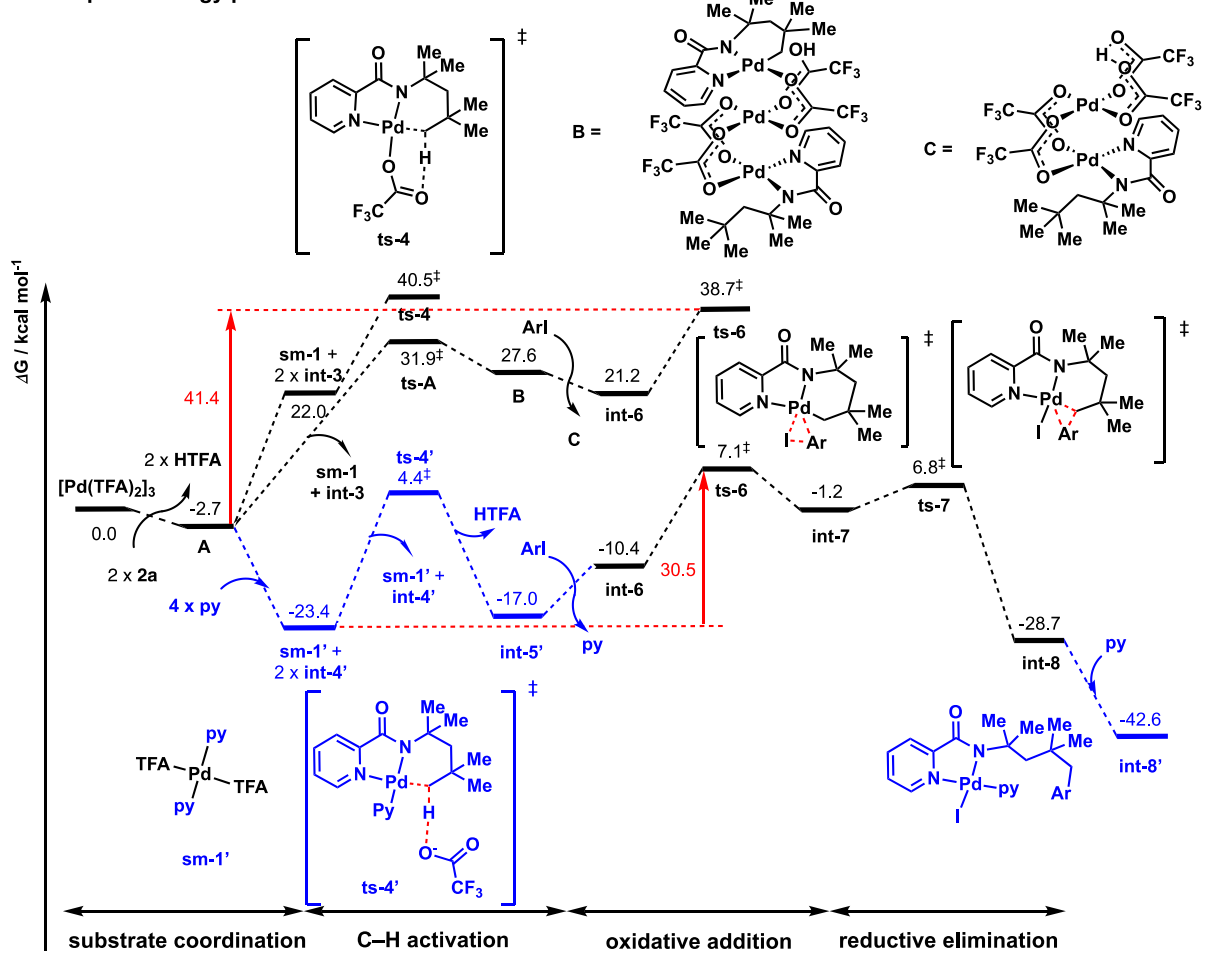


Figure S4. Optimized structures of (a) monomeric, (b) dimeric and (c) trimeric palladium trifluoroacetate.

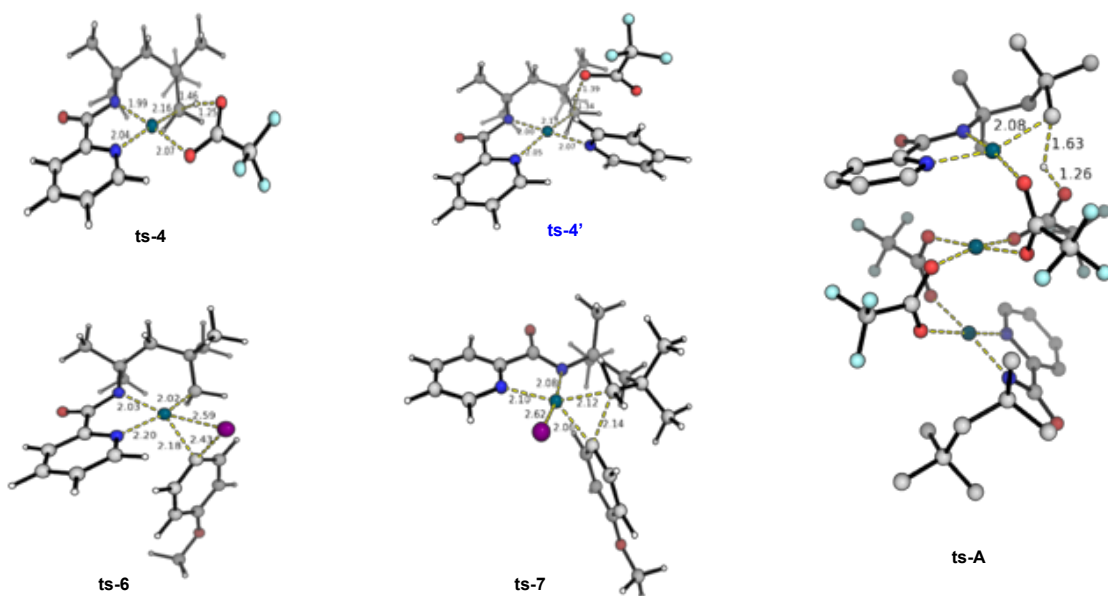
II.3 Trinuclear pathway for Pd(II) catalysis – first arylation

Mononuclear Pd-catalyst gave an overall activation barrier of 28.2 kcal mol⁻¹ without any ligand, with oxidative addition (OA) being the r.d.s; this barrier increased to 32.5 kcal mol⁻¹ with pyridine coordination (Figure S1). This is inconsistent with the experimental observation that the reaction proceeded faster with a higher yield in pyridine ligand. Considerations of trinuclear pathway was necessary. The overall Gibbs free energy profile for the reaction starting from trimeric Pd-catalyst is shown in Figure S5A. With pyridine, the dissociation of the trimeric complex was favourable. The C–H activation step is reversible both in the presence and absence of pyridine ligand, in excellent agreement with experimental evidence using kinetic isotope effect and H/D exchange studies. The OA/RE steps were both catalysed by monomeric form of palladium catalyst, since Pd(II) metal is

A. Computed energy profile for the reaction of 2a



B. Transition structures



C. Proposed catalytic cycle

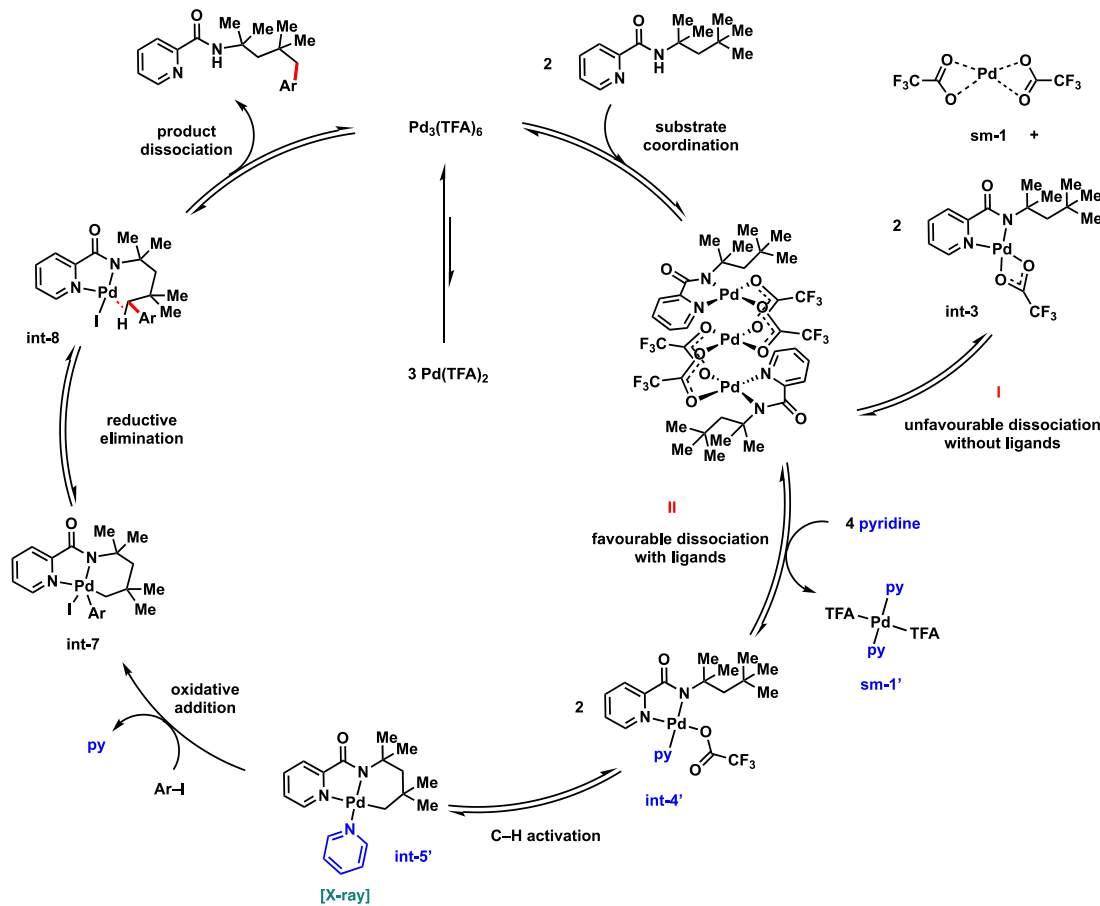


Figure S5. (a) Computed Gibbs free energy profile for first arylation in the absence (black) and presence (blue) of pyridine ligand with trimeric palladium trifluoroacetate catalyst as starting material. All values are quoted in kcal mol⁻¹. (b) Key transition structures, bond distances are given in Å. (c) Proposed mechanistic cycle.

tetra-coordinating and there needed to be vacant coordination site on the metal for the incoming aryl iodide to be added. As we can see from the energy profile, the activation barrier in the absence of pyridine ligand is 41.4 kcal mol⁻¹ whereas this decreases to 30.5 kcal mol⁻¹ in the presence of pyridine ligand. Note that it is the exergonic formation of **sm-1'** that favours the reaction.³² This corroborated well with the experimental observation that the reaction yield improved in the presence of pyridine ligand, albeit the reaction can also occur in the absence of pyridine.

A closer look at the C–H activation step in the presence of pyridine revealed that this step was reversible when pyridine acted as a Pd-coordinating ligand (**ts-4'**). The activated complex (**int-5'**, X-ray structure in the absence of aryl iodide) was all thermally uphill. Importantly, the subsequent OA of aryl iodide into Pd metal (**ts-6**) had a higher activation barrier than the reverse step (Figure 1D). Our calculations support the experimental kinetic isotope effect and H/D exchange studies that C–H activation step was unlikely the r.d.s. for this reaction. The subsequent OA occurred in the absence of pyridine ligand, consistent with the observation that

complexes with even number of coordination undergo OA/RE less readily than those with odd number of coordination.²³ The aryl iodide inserted oxidatively to form a pentavalent Pd(IV) intermediate **int-7** that is highly endergonic. This intermediate underwent RE, reverting the metal from Pd(IV) to Pd(II) in the arylated product. It is worth noting that the OA and RE steps have comparable Gibbs energies of activation, making it difficult to pinpoint exactly which of these steps is rate-determining; RE step, in fact, became the r.d.s for second and third arylation (Section II.4).

The overall first arylation is reversible without pyridine ligand but irreversible with pyridine ligand, since structure **int-8** can be further stabilised by pyridine coordinating to the Pd(II) metal to give **int-8'**, thereby stabilising the end product. With pyridine coordination to the end product, the first arylation is thermodynamically favoured.

II.4 Second and third arylation

The steps for second arylation were similar to those of first arylation except now that two diastereomers were possible; these conformations were thoroughly explored (Figure S7). The overall Gibbs free energy profile for diastereomer 1 is shown in Figure S6. Comparing to first arylation, the RE step had slightly higher activation barrier than OA, in contrast to first arylation, suggesting that these two steps were very close in activation barriers. Without pyridine, the energy span for second arylation was 41.3 kcal mol⁻¹ (between structures **A** and **ts-12**), which was comparable to the energy span for first arylation (at 41.4 kcal mol⁻¹), making second arylation comparable in the absence of pyridine ligand. Both first and second arylations in the absence of pyridine ligand were reversible, resulting in small mono:di-arylation selectivity. With pyridine, the end product of first arylation got coordinated to give **int-8'** with much lowered energy. This stabilisation of first arylation product by pyridine coordination increased the energy span for second arylation to 50.1 kcal mol⁻¹, making it thermally unfeasible. This explains the experimental observation that the presence of pyridine favours mono:di-arylation in favour of mono-arylated product.

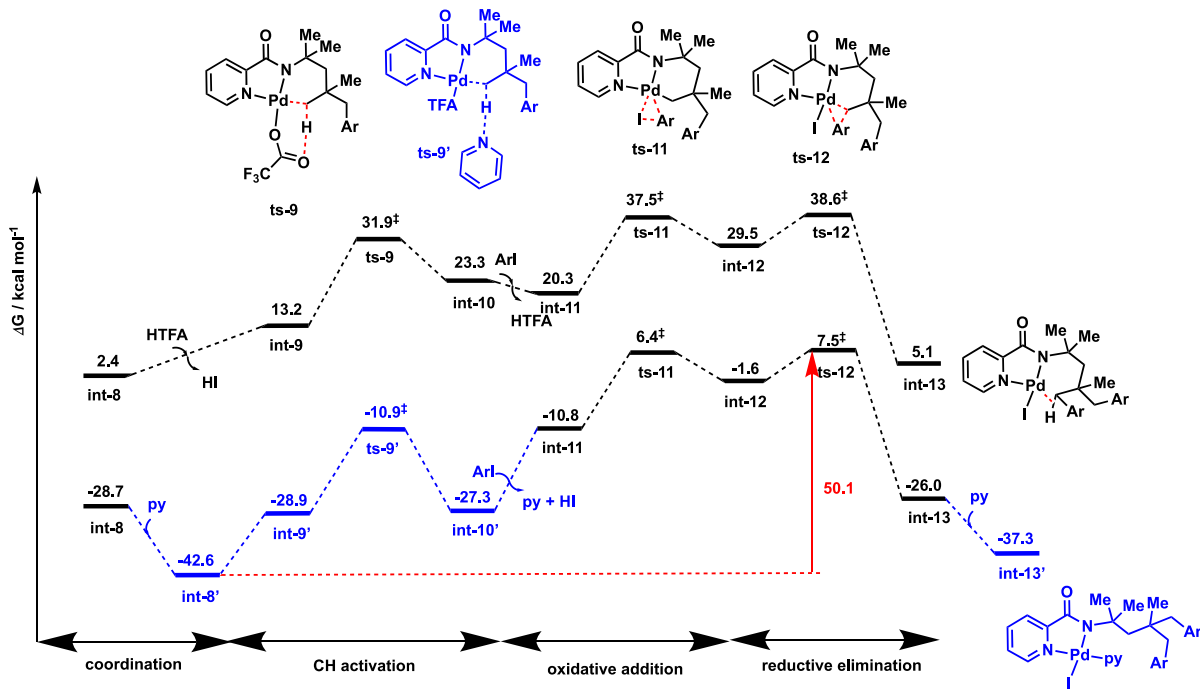
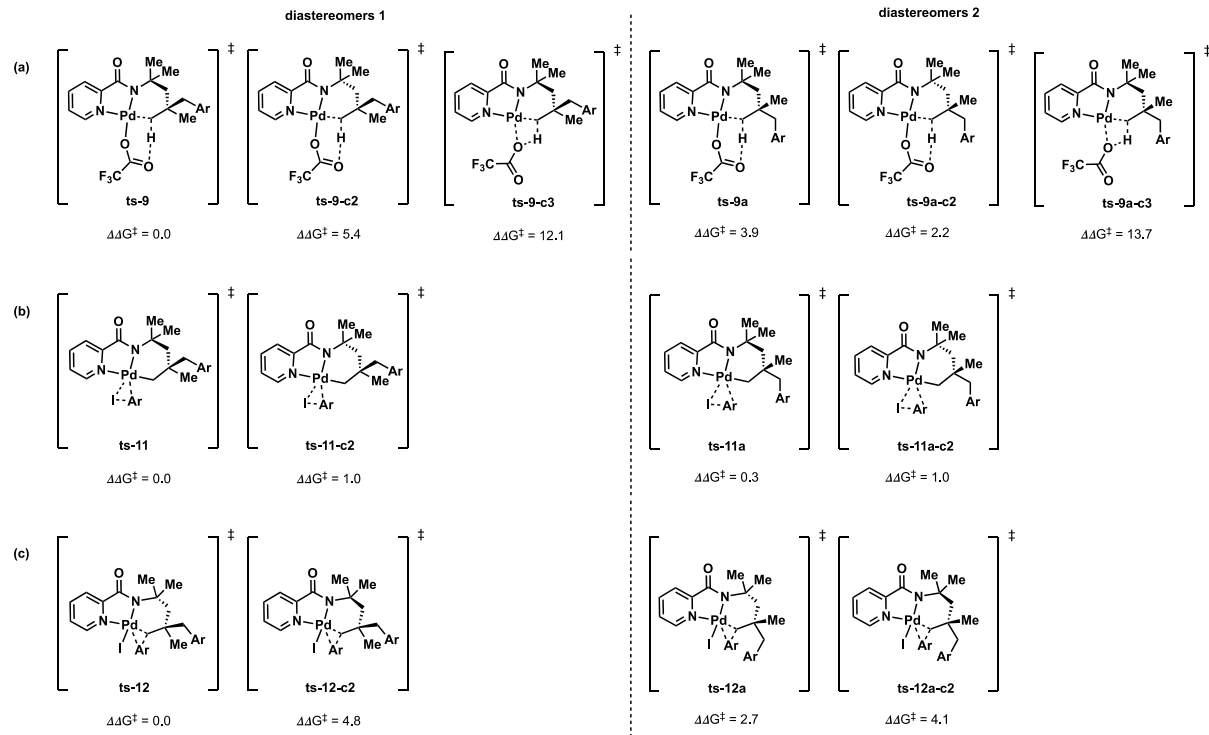


Figure S6. Computed Gibbs free energy profile for second arylation in the absence (black) and presence (blue) of pyridine ligand with trimeric palladium trifluoroacetate catalyst as starting material. All values are quoted in kcal mol⁻¹. Note that only one stereoisomer (site of arylation) is shown, the other stereoisomer was calculated and found to have similar results.



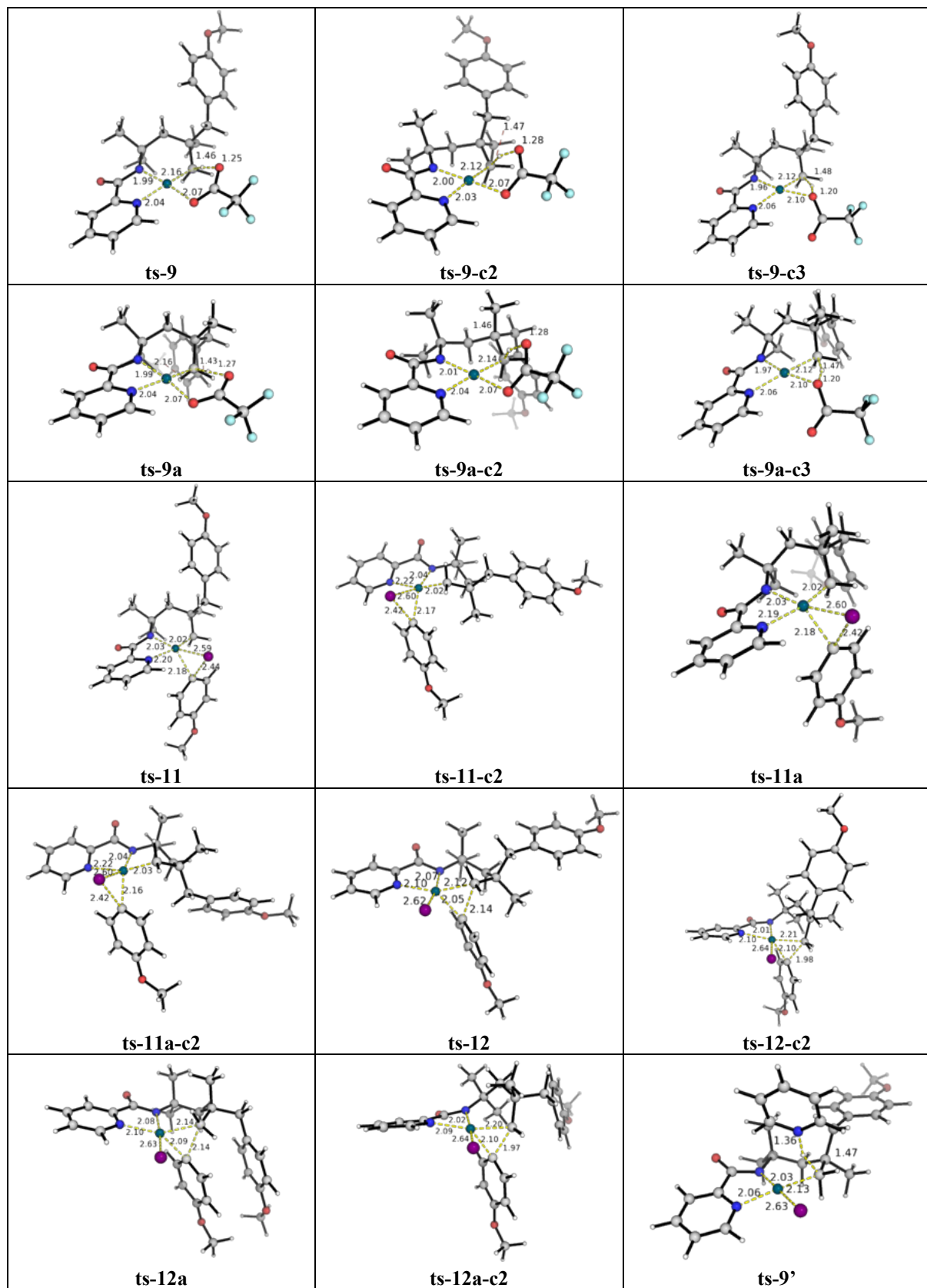


Figure S7. Top: Relative activation energies for different conformations of (a) C–H activation, (b) oxidative addition and (c) reductive elimination TSs for second arylation. Bottom: Optimised TS structures. Key bond distances are given in Å.

The steps for third arylation was similarly analysed with all possible TSs in different conformations given in Figure S9; the Gibbs free energy profile for the lowest-energy pathway is shown in Figure S8 below. The energy span for third arylation without pyridine ligand was 43.9 kcal mol⁻¹ (between structures A and ts-17), whereas this was 47.8 kcal mol⁻¹ with pyridine. We predict that di- and tri-arylation would be achieved more easily in the absence, rather than the presence, of the pyridine ligand.

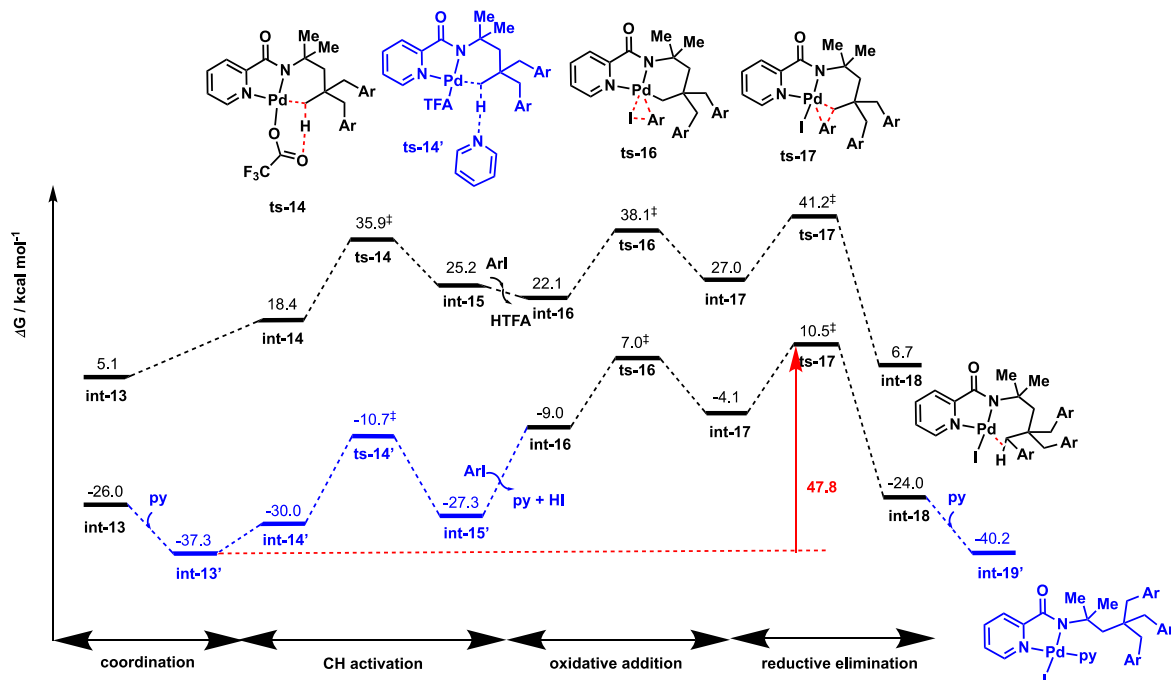
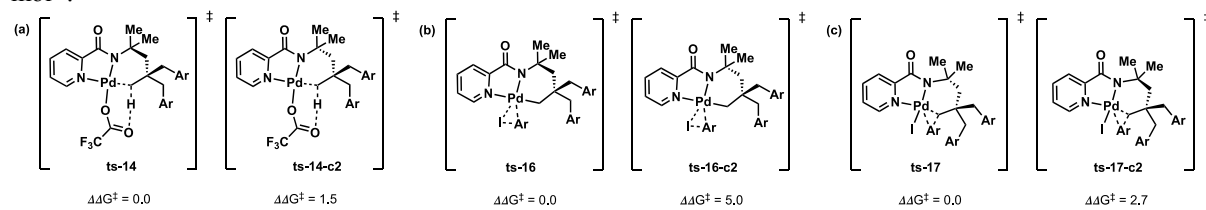


Figure S8. Computed Gibbs free energy profile for third arylation in the absence (black) and presence (blue) of pyridine ligand with trimeric palladium trifluoroacetate catalyst as starting material. All values are quoted in kcal mol⁻¹.



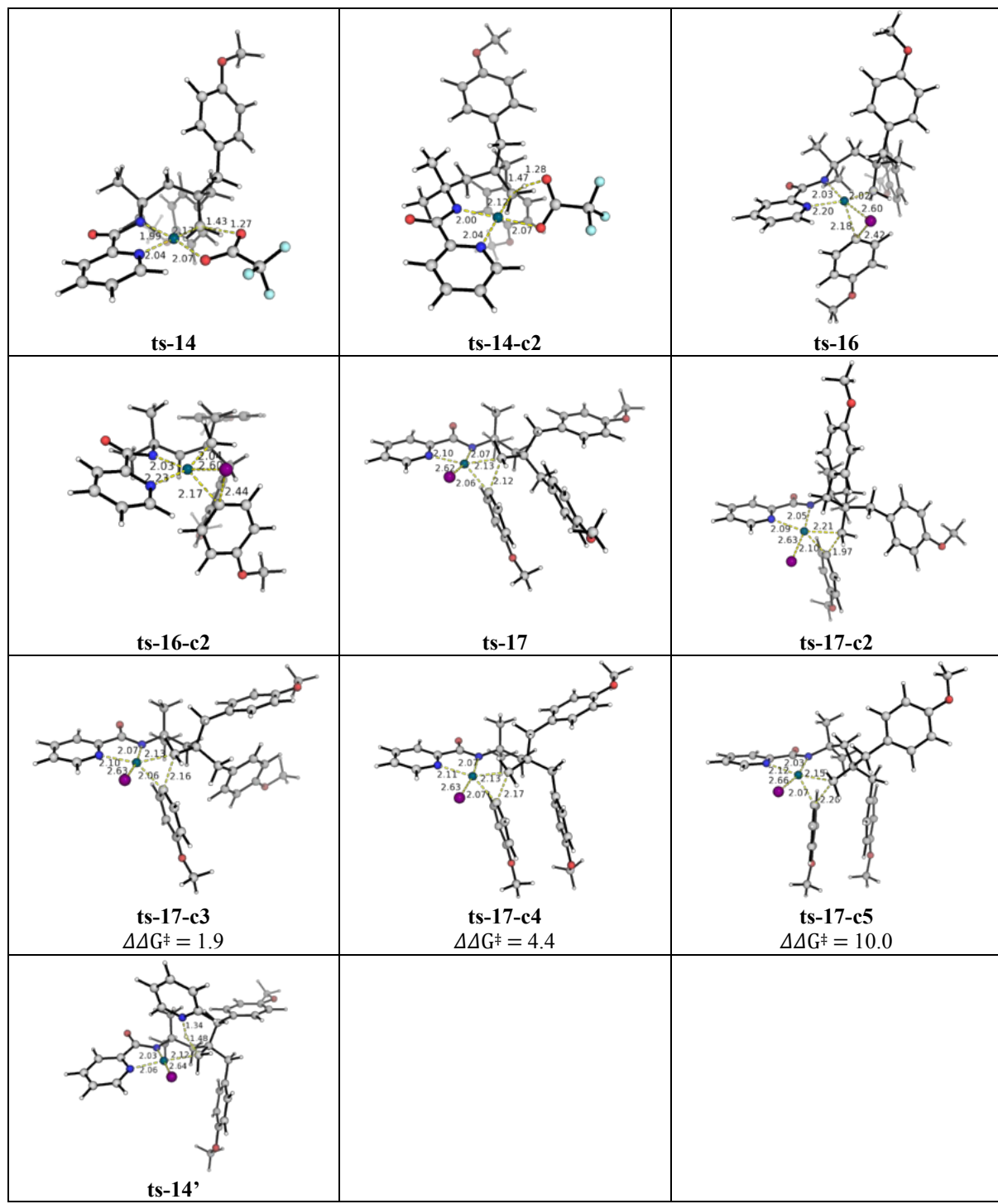


Figure S9. Top: Relative activation energies for different conformations of (a) C–H activation, (b) oxidative addition and (c) reductive elimination TSs for third arylation. Bottom: Optimised TS structures. Key bond distances are given in Å.

II.5 Effects of directing groups

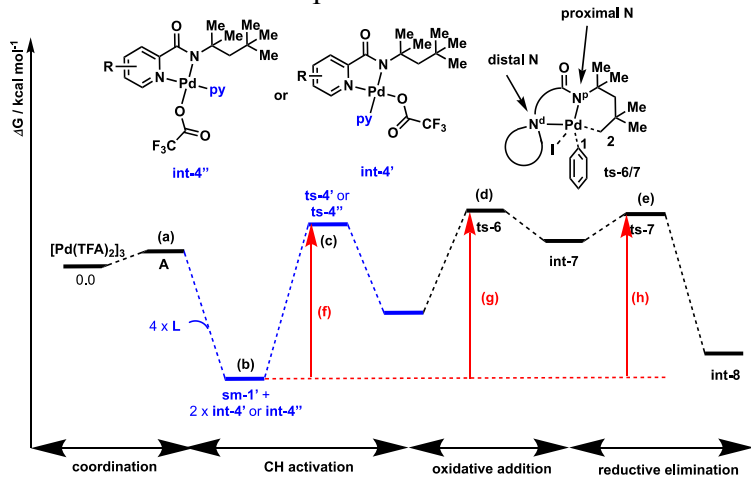
Table S1 gives the reaction barriers for CH activation, OA and RE steps. Either OA or RE step was r.d.s. depending on substrate structure. Structures **PG1** and **PG4-PG6** had the lowest activation barriers; they were predicted to be the best directing group for arylation and to give similar yields. Experimentally, **PG5/PG6** gave much lower yield than **PG1** and **PG4**. This could be because the extra N atom in the heteroaromatic rings in **PG5/PG6** interact with other molecules (such as solvent) to impede the OA and RE steps. The strong coordinating ability of the extra N-atom could also outcompete substrate binding sites and deactivate catalytic activity. Structures **PG2/PG3/PG8**, with substitutents at the *ortho*-position relative to the N-atom in the pyridine ring, all had higher activation barriers than **PG1**, indeed, these gave very poor yield.

Analysis of the HOMO of the TSs for both OA and RE steps for all PGs indicated that the electron distributions were rather similar (Figures S10). The key geometrical parameters in these TSs showed that the RE TSs had very similar geometries; the OA TSs had varying Pd-N^d bond distances, implicating a different degree of electron donation from the lone pair on the directing groups to Pd metal. **PG2/3/8** all had longer Pd-N^d bond distances (2.25-2.28 Å) than that in **PG1** (2.20 Å). A quantitative NBO analysis of second-order perturbative stabilisation energy indicated that these TSs were stabilised to a lesser extent than **PG1** (Table S3). In addition, the substituents in these PGs were in *ortho*-position relative to N-atom of the pyridyl ring, giving rise to unfavourable sterics when these substituents interacted with the aryl-group of the iodoanisol that is being oxidatively added. This is confirmed by the NCI plots as well as van der Waals pictures of these PGs (Figure S11, S12). For **PG7**, the palladacycle formed [6,6]-rings, which, although had similar bond distances in the TS compared to **PG1** (Table S2), introduced very unfavourable ring strain and repulsive interactions (Figure S11, S12). The [6,6]-palladacycle is disfavoured and this is confirmed by various other studies.³³⁻⁴⁰

Both NBO analyses and NCI plots for **PG4-PG6** indicated similar electronic and steric interactions to those in **PG1**, implicating similar yields possible. However, the lone pair on the heterocyclic N-atom in **PG5** had unfavourable repulsive interaction with the amide oxygen atom (as indicated by the NCI plot in Figures S11, region 1), therefore destabilising the TS more than in **PG6**, therefore giving lower experimental yield. **PG4** had F atom *meta*- to the directing N atom, thereby, out of steric clashes with incoming aryl iodide that was being added. These analyses indicated that steric factors play a dominant role in influencing the stability of the TSs.

For PGs that chelate to Pd metal in a [5,6]-fused fashion, the presence of a substituent at the *ortho*-position relative to the ring N-atom, regardless of its electronics (electron-withdrawing -F group in **PG2** and electron-donating -OMe group in **PG3**, and benzene ring as part of quinoline in **PG8**), rendered the PG ineffective. A detailed analysis of the stereoelectronics of these PGs suggests that the electron distributions in the HOMO of the OA and RE transition states were rather similar (Figure S10). NBO charges on Pd metal in OA TSs with different PGs showed that **PG2, PG4-PG6** all had smaller charge, ranging from +0.201e to +0.204e, than **PG1**, at +0.208e (Table S3). In these PGs, the Pd had low valency/oxidation state and higher electron density, favouring the oxidative addition of incoming aryl iodide. In addition, the metal center was stabilized by lone pair donation from amide N atom the most in **PG1/PG4/PG6**, as shown by the largest perturbative E2 stabilisation energy values in NBO analyses (Table S3); these electronic

stabilisation greatly favoured oxidative addition as Pd-metal cycled from Pd(II) to Pd(IV). Steric factors play an important role in the OA step. The



PGs	Expt Yield	(a)	(b) ^α	(c) ^α	(d)	(e)	(f) or (g) or (h) ^β
PG1	77%	-2.7	-25.4°	3.9''	7.1	6.8	32.5 ^g
PG2	0%	11.5	-14.3°	14.3°	17.7	21.8	36.1 ^h
PG3	0%	2.9	-20.2°	9.5°	13.5	16.2	36.4 ^h
PG4	75%	1.1	-22.5''	7.9''	11.2	11.4	33.9 ^h
PG5	7%	2.1	-23.1''	6.9''	10.2	9.9	33.3 ^g
PG6	25%	4.0	-21.8''	8.4''	12.0	12.4	34.2 ^h
PG7	0%	3.5	-23.1''	12.6''	15.9	28.3	51.4 ^h
PG8	10%	1.3	-22.7''	8.4''	12.9	15.4	38.1 ^h

α The most stable structure (**4'** or **4''**) is taken as the one with the lowest Gibbs free energy. The superscript in each value indicates which of these two (' for **4'** and '' for **4''**) are taken.

β The maximum energy span takes the value of (f) if C–H activation via CMD is the RDS and the value of (g) if oxidative addition is the RDS and the value of (h) if reductive elimination is the RDS.

Table S1. The reaction barriers for different directing groups used in the arylation reaction.

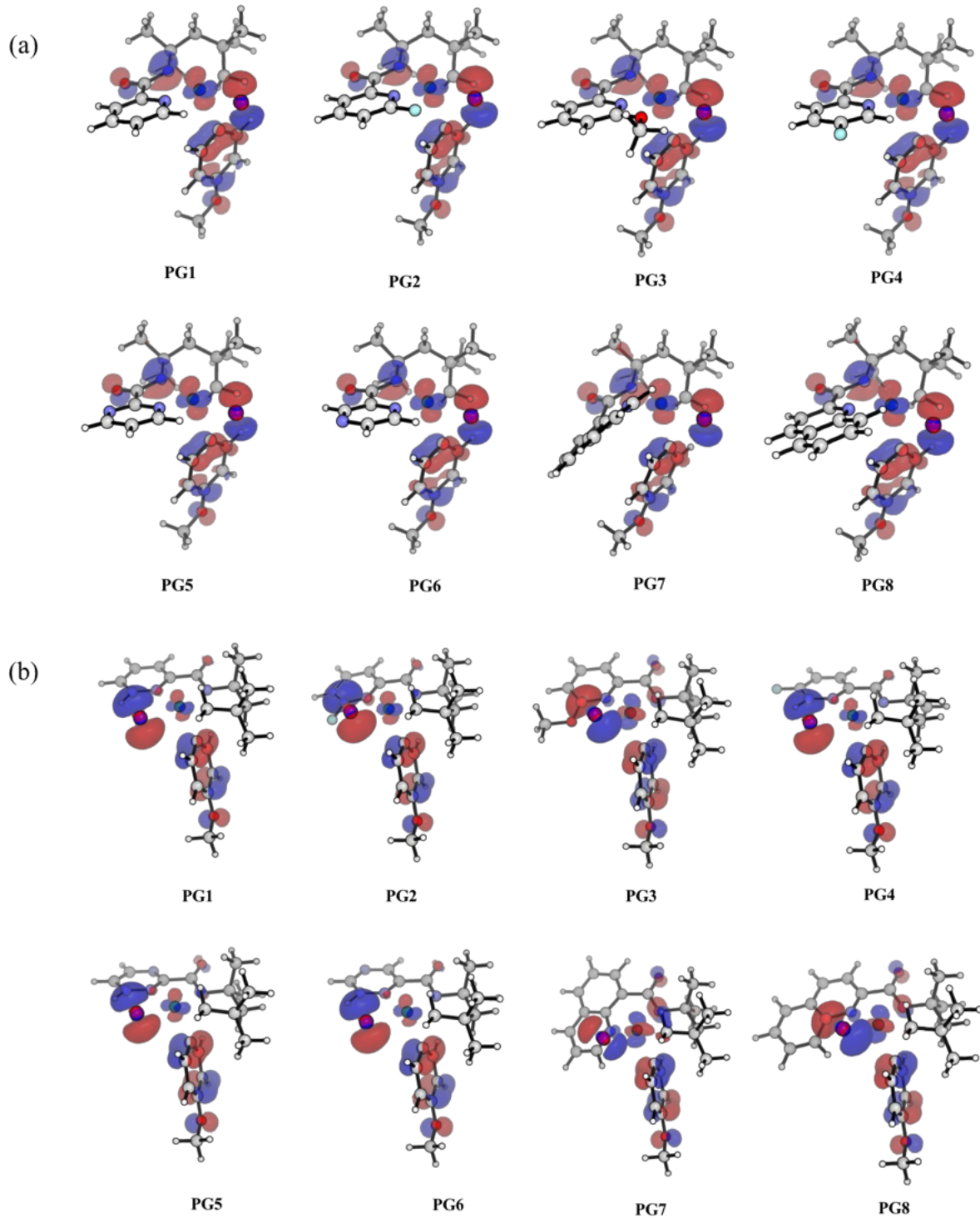


Figure S10. HOMO of TSs for (a) oxidative addition and (b) reductive elimination at an isovalue of 0.05.

incoming Ar–I groups increased steric crowding, therefore, any steric bulk hindering the incoming aryl iodide would disfavour this step. Evidently, non-covalent interactions (NCI) plots and van der Waals surface visualisations (Figures S11, S12) showed that the presence of a substituent at the *ortho*-position relative to the ring N-atom (**PG2/PG3/PG8**) gave rise to unfavourable repulsion, thus heightening the barrier of activation. For the PG that chelated to Pd metal in a [6,6]-fused fashion (**PG7**), similar analysis suggests that the unfavourable ring twisting in these TSs gave rise to augmented repulsion between the substrate and incoming

Oxidative addition TSs								
	Bond distances / Å					Bond angles / °		
Structure	Pd-N ^p	Pd-N ^d	Pd-I	Pd-C1	Pd-C2	N ^p -Pd-I	C2-Pd-N ^d	I-Pd-C1
PG1	2.03	2.20	2.59	2.18	2.02	163.2	168.2	60.4
PG2	2.04	2.26	2.59	2.14	2.02	161.1	165.3	63.1
PG3	2.04	2.25	2.60	2.14	2.03	162.4	164.9	62.3
PG4	2.03	2.21	2.59	2.18	2.02	162.8	168.2	60.7
PG5	2.02	2.20	2.60	2.18	2.02	162.4	168.0	60.6
PG6	2.03	2.21	2.59	2.17	2.02	162.6	168.1	61.2
PG7	2.03	2.22	2.59	2.15	2.03	173.2	171.0	62.8
PG8	2.03	2.28	2.60	2.15	2.03	166.6	163.8	61.6

Reductive elimination TSs								
	Bond distances / Å					Bond angles / °		
Structure	Pd-N ^p	Pd-N ^d	Pd-I	Pd-C1	Pd-C2	N ^p -Pd-I	C2-Pd-N ^d	C2-Pd-C1
PG1	2.08	2.10	2.62	2.06	2.12	166.7	157.2	61.5
PG2	2.08	2.11	2.62	2.06	2.12	160.5	162.7	60.8
PG3	2.08	2.10	2.63	2.05	2.12	159.0	162.4	60.9
PG4	2.08	2.10	2.62	2.06	2.12	167.1	156.8	61.5
PG5	2.07	2.10	2.62	2.06	2.12	167.0	158.1	61.6
PG6	2.08	2.10	2.62	2.06	2.12	167.2	156.6	61.8
PG7	2.06	2.09	2.63	2.07	2.12	158.6	175.1	60.1
PG8	2.07	2.10	2.63	2.05	2.12	157.7	164.1	60.9

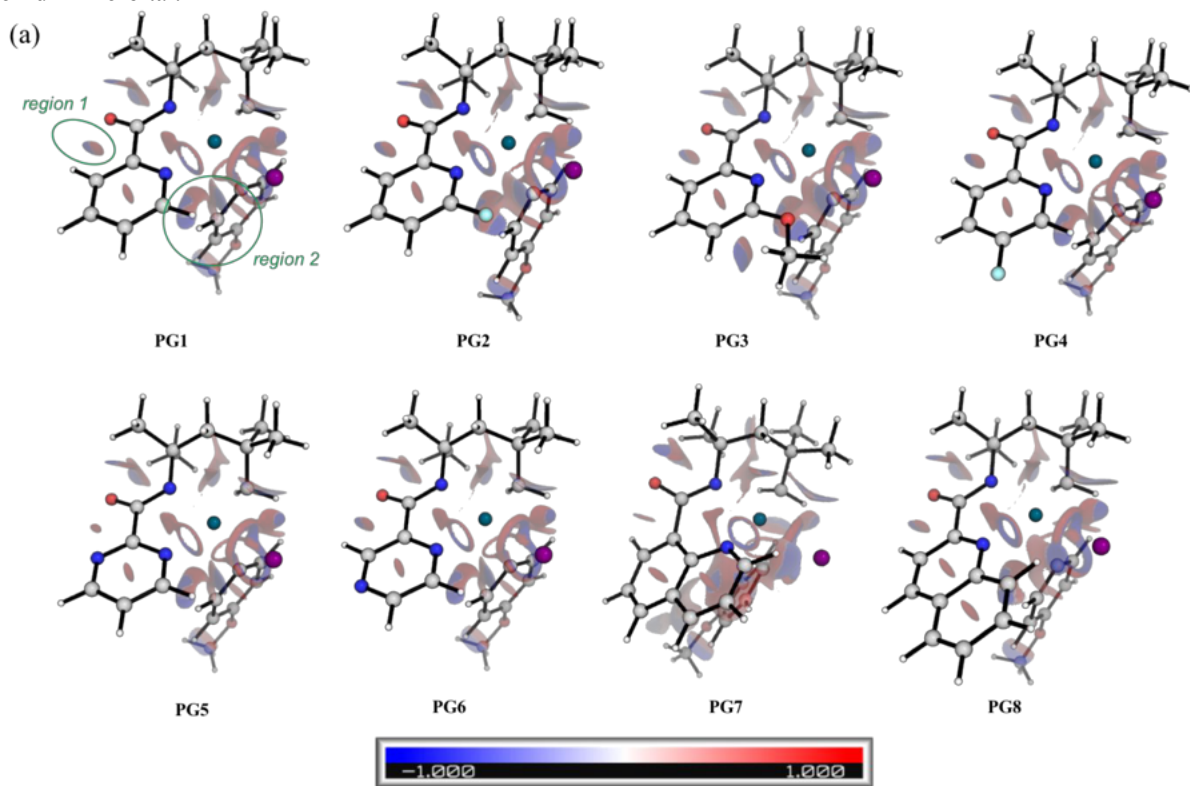
Table S2. Key geometrical parameters for the TSs in the oxidative addition and reductive elimination steps.

Oxidative addition TSs								
	NBO charge q/e						Largest E ₂ from donor LP to Pd LP*/kcal mol ⁻¹	
Structure	Pd	N ^p	N ^d	I	C1	C2	N ^p	N ^d
PG1	0.208	-0.586	-0.417	0.187	-0.044	-0.433	38.50	38.02
PG2	0.201	-0.595	-0.446	0.173	-0.030	-0.406	4.56	37.10
PG3	0.216	-0.595	-0.442	0.167	-0.031	-0.417	4.39	37.11
PG4	0.204	-0.588	-0.397	0.189	-0.045	-0.427	38.41	37.95
PG5	0.201	-0.589	-0.443	0.186	-0.049	-0.433	4.65	40.64
PG6	0.202	-0.588	-0.385	0.184	-0.041	-0.423	38.14	38.18
PG7	0.213	-0.598	-0.428	0.141	0.001	-0.424	5.57	35.91
PG8	0.215	-0.591	-0.407	0.160	-0.030	-0.413	4.53	33.03

Reductive elimination TSs

Structure	NBO charge q/e						Largest E_2 from donor LP to Pd LP* / kcal mol $^{-1}$	
	Pd	N^p	N^d	I	CI	C2	N^p	N^d
PG1	0.227	-0.567	-0.395	-0.202	0.034	-0.322	5.74	47.13
PG2	0.213	-0.567	-0.432	-0.169	0.043	-0.345	7.67	44.48
PG3	0.236	-0.566	-0.426	-0.205	0.045	-0.352	6.46	46.96
PG4	0.222	-0.568	-0.378	-0.194	0.033	-0.319	5.53	45.07
PG5	0.221	-0.569	-0.425	-0.209	0.034	-0.322	83.25	47.63
PG6	0.217	-0.568	-0.367	-0.191	0.033	-0.316	80.40	45.23
PG7	0.245	-0.572	-0.398	-0.171	0.062	-0.398	77.96	43.75
PG8	0.228	-0.562	-0.381	-0.189	0.046	-0.357	70.58	45.11

Table S3. NBO charge and the largest perturbative E2 stabilisation energy from the lone pair (LP) donation from N to Pd LP* orbital.



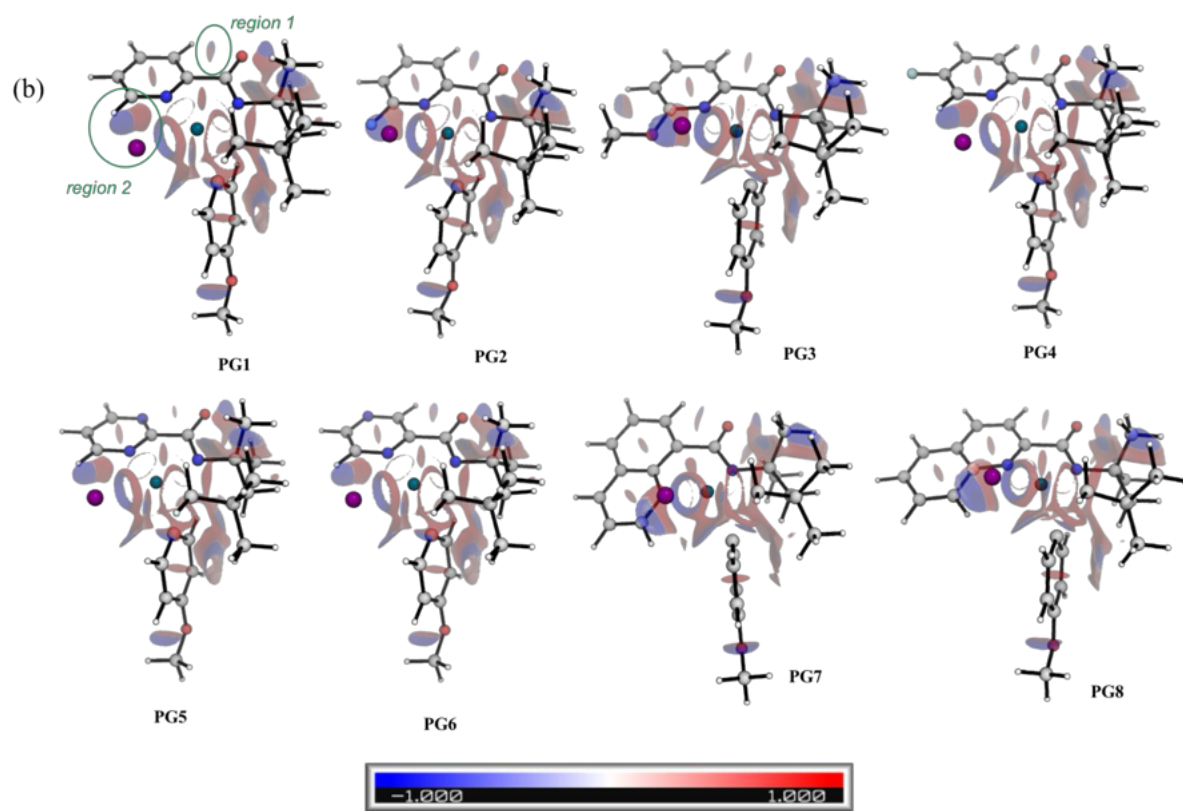


Figure S11. NCI plots of TSs for (a) oxidative addition and (b) reductive elimination at an isosurface value of 0.05.

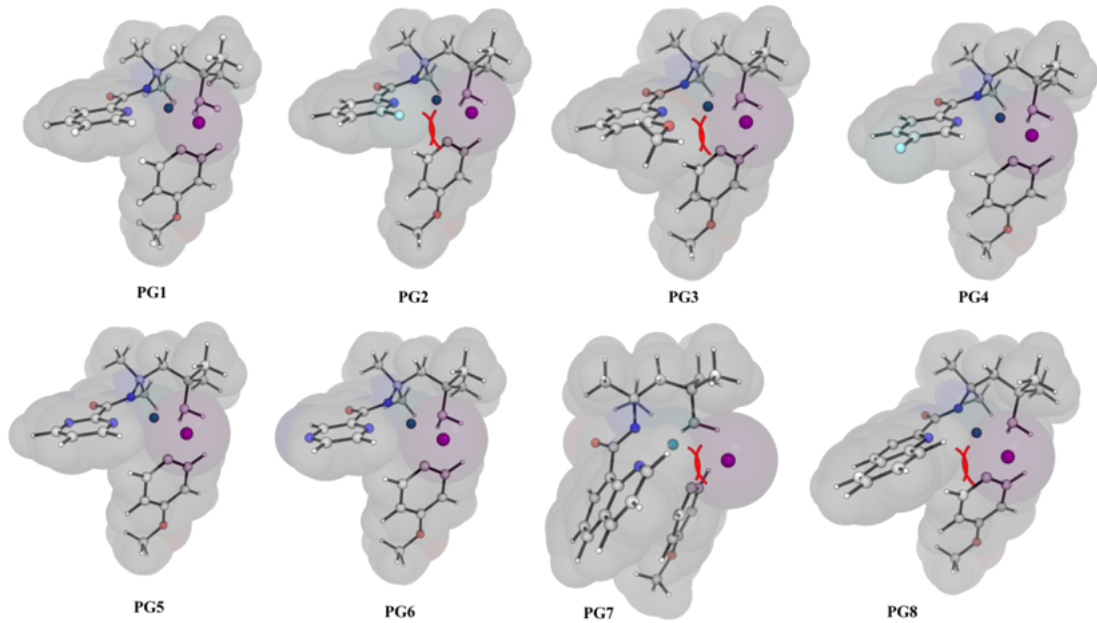


Figure S12. van der Waals surfaces visualisation of oxidative addition TSs. Steric clashes between the substituents *ortho*- to pyridyl ring and the incoming aryl iodide (**PG2/3/8**) can clearly be seen.

aryl iodide and subsequent enhanced barrier heights, rendering the PG ineffective (NCI plot, Figure S11). The [6,6]-palladacycle is known to be unfavourable,^{47,48} due to steric constraints seen here. The barrier heights correlated well with the sterics involved in the TSs (Table S1). **PG6** (and **PG5**), although satisfying the stereoelectronic constraints on the rate-determining OA step, performed badly experimentally, possibly due to the coordinating ability of the heterocycles to outcompete substrate binding and deactivate catalytic activity or to bind to extra molecules (other ligand/solvent molecules) that impede OA/RE steps in ways that were not captured in the present considerations.

III. Computational study of *N*-(4-methylpentan-2-yl)picolinamide (substrate **3a**)

III.1 Reaction pathway involving mononuclear Pd(II) catalyst

Experimentally, it was found that the reaction mechanism changed when the substrate changed from **2a** to **3a**. Both experiments and calculations revealed that when structure **2a** was used, the C–H activation step was reversible and non-rate-determining. However, when structure **3a** was used, C–H activation step became rate-determining and the use of pyridine ligand **L1** did not give any yield. A screening of ligands found that using pyridone ligand **L14** (where R = Bn protecting group) gave good yield in a reaction condition that required higher temperature than the substrate **2a**. Note that C–H activation step for substrate **3a** is 3.9 kcal mol^{−1} ($\Delta\Delta G^\ddagger$) higher than for **2a**, as expected, since the lack of Thorpe-Ingold effect in **3a** makes the C–H activation step more difficult.

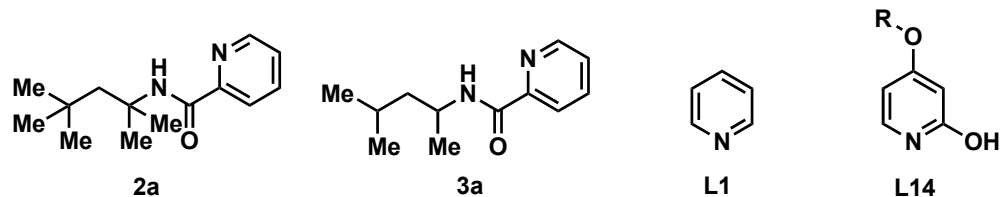


Figure S13 gives the energy profile for this reaction involving mononuclear catalyst in the presence and the absence of ligand **L14** (for computational study, we used R = Me group). The energy barrier in the absence of ligand is 33.1 kcal mol^{−1} whereas this barrier increased to 43.2 kcal mol^{−1} in the presence of ligand, inconsistent with experimental observation that this reaction could not occur in the absence of ligand; it could only occur in the presence of ligand. Trinuclear pathway was next explored.

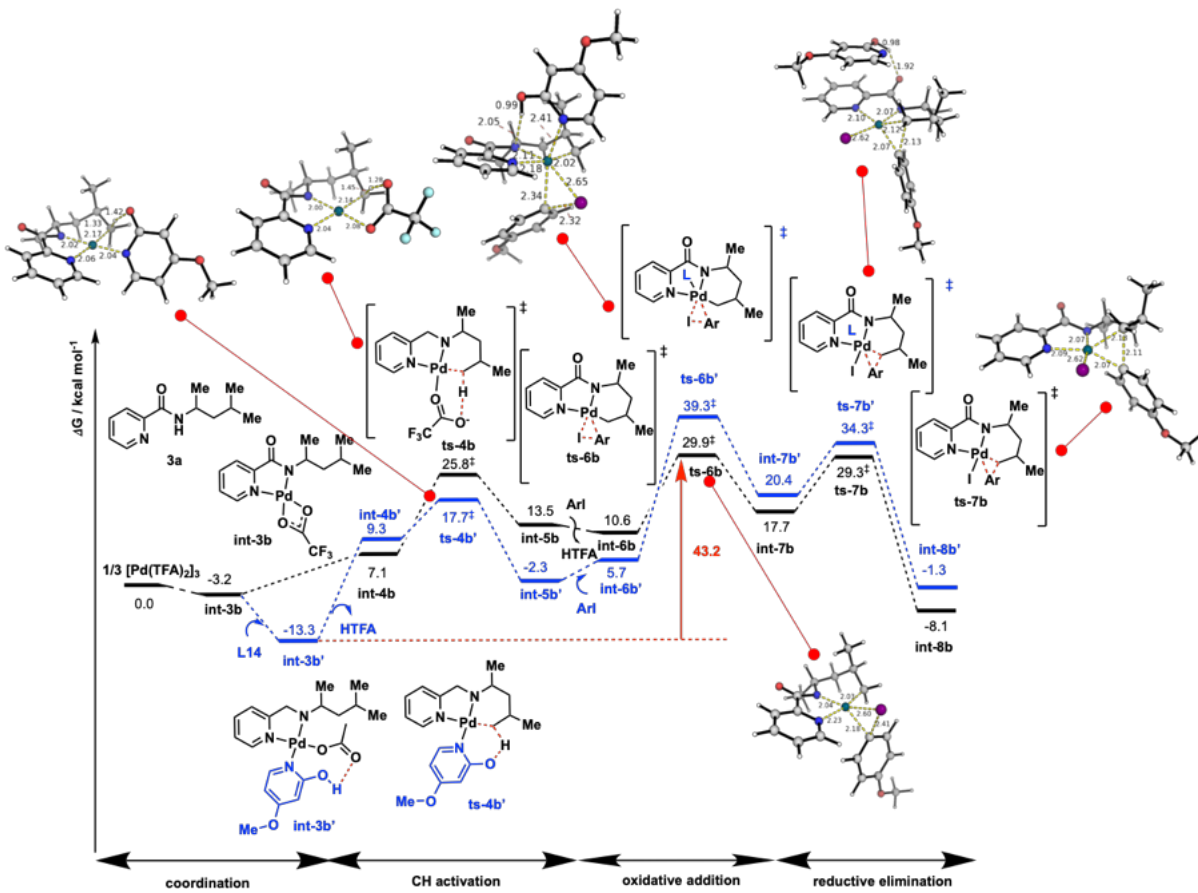


Figure S13. Computed Gibbs free energy profile for first arylation in the absence (black) and presence (blue) of pyridone ligand involving mononuclear Pd-catalyst. All values are quoted in kcal mol⁻¹. Bond distances are quoted in Å.

III.2 Reaction pathway involving trinuclear Pd(II) catalyst

The catalyst involved was trinuclear in nature as previously. Taking the trimeric $[\text{Pd}(\text{TFA})_2]_3$ as the starting material, the Gibbs energy profile is given in Figure S14. In the absence of any ligand (the black pathways on top), the dissociation of trimeric $\text{Pd}_3(\text{TFA})_6$ catalyst complex to its monomeric forms that further underwent OA/RE was thermally inaccessible, requiring

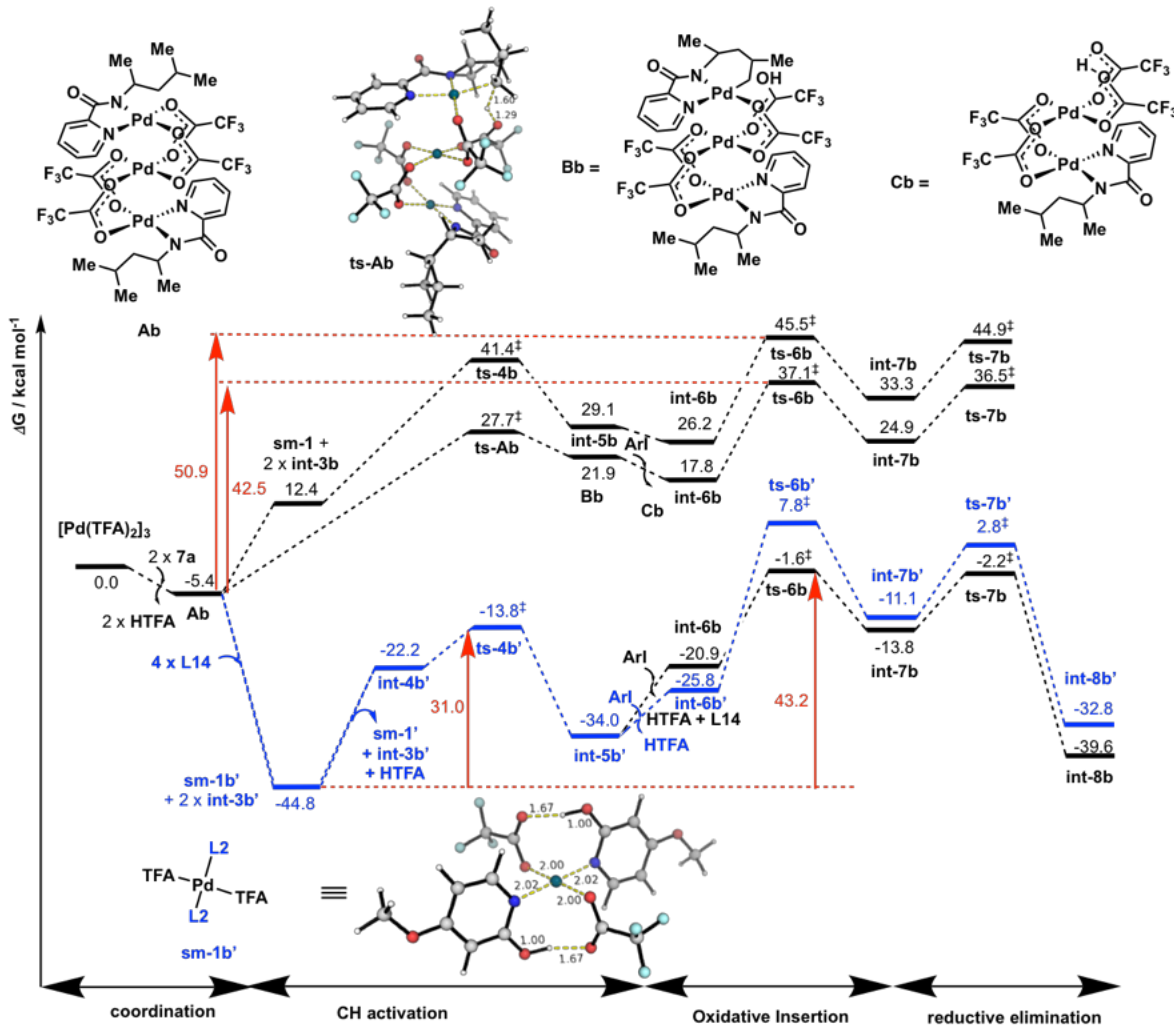


Figure S14. Computed Gibbs free energy profile for first arylation in the absence (black) and presence (blue) of pyridone ligand with trimeric palladium trifluoroacetate catalyst as starting material. All values are quoted in kcal mol⁻¹. Bond distances are quoted in Å.

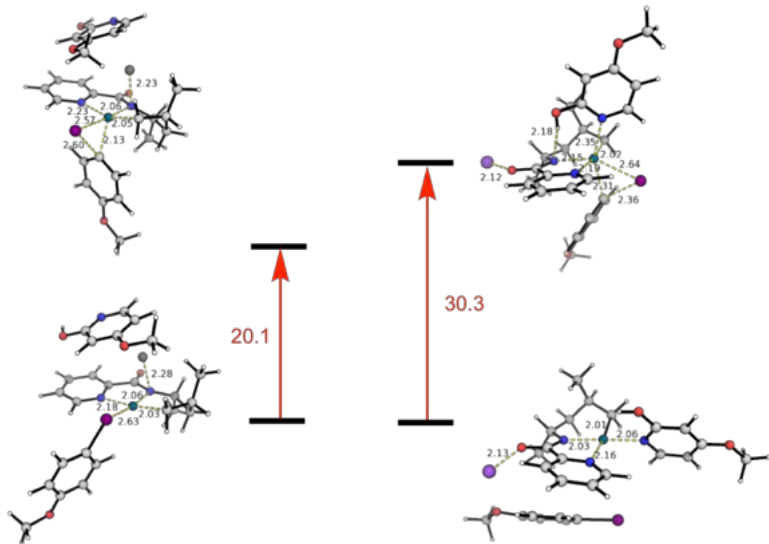


Figure S15. Optimised structures involving cationic species. Left: with silver cation; right: with sodium cation. Energy barriers are quoted in kcal mol⁻¹. Bond distances are quoted in Å.

energy to overcome a very high reaction barrier of 50.9 kcal mol⁻¹. The direct C–H activation via CMD of the trimeric complex **Ab** was more favourable than its dissociation, giving an overall activation barrier of 42.5 kcal mol⁻¹. With pyridone ligand **L14**, the trimeric complex **Ab** favourably dissociated into its monomeric forms **sm-1b'** and **int-3b'**. This was followed by a ligand-assisted CMD C–H activation **ts-4b'**. The subsequent OA and RE steps were, however, higher than the C–H activation steps, similar to substrate **2a** found earlier. We found that the pyridone ligand **L14** were not directly involved in either OA/RE steps as these (**ts-6b'** and **ts-7b'**) had higher activation barriers than the steps without pyridone ligand (**ts-6b** and **ts-7b**). Additionally, the r.d.s. from this energy profile was also the OA step, as in substrate **2a**. It conflicts the experimentally finding that the C–H activation step was the r.d.s.. We considered the possible pathways involving cationic intermediates in the OA step to see if this provides an alternative pathway.^{9,41} The introduction of either Ag⁺ or Na⁺ cation in the presence of ligand **L14** were considered separately. We found that the activation barrier for OA was 30.3 kcal mol⁻¹ with Na⁺ cation and 20.1 kcal mol⁻¹ with Ag⁺ cation, relative to the cationic intermediates, implicating possible Ag⁺ cation participation (Figure S15). Since it is difficult to compare species with different overall charges due to solvation energies involved,^{42,43} we considered a heterodimeric catalytic species involving silver cation for OA/RE steps in neutral pathways, in a fashion similar to the heterodimeric Pd–Ag catalytic species considered for C–H activation step by Houk and Schaefer.^{44,45} The overall energy profile for the involvement of silver carbonate is shown in Figure S16.

III.3 Reaction pathway involving silver carbonate as co-ligand

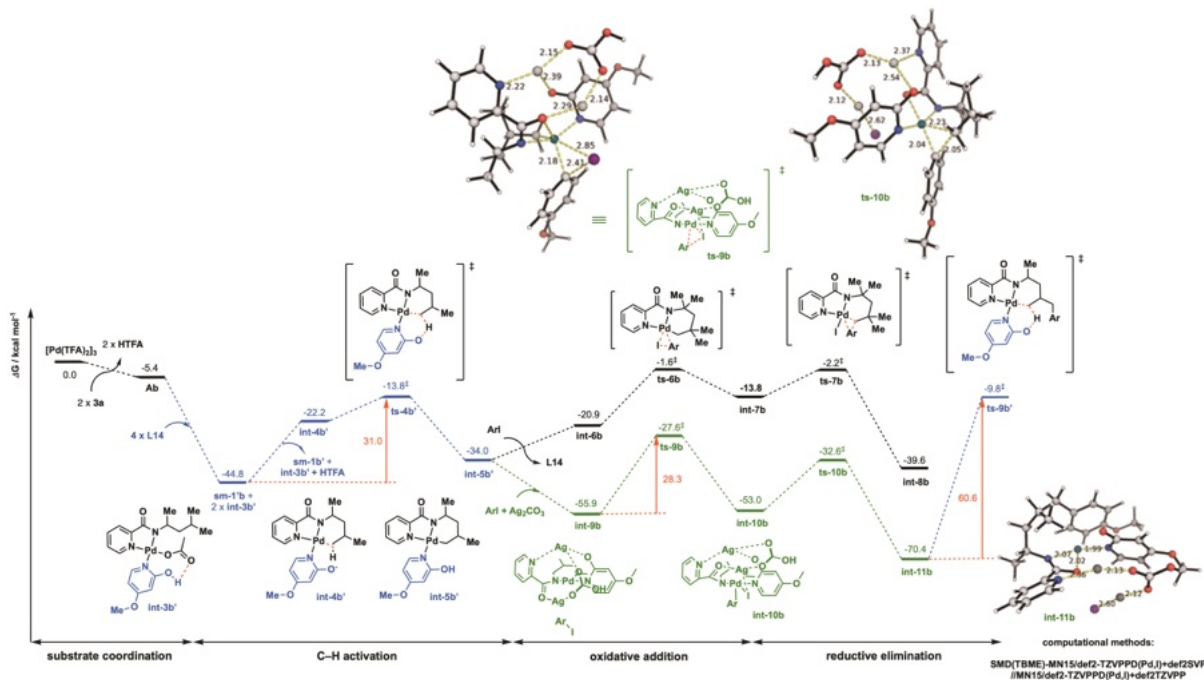


Figure S16. Computed Gibbs free energy profile for first arylation in the presence of pyridone ligand **L14** and silver carbonate with trimeric palladium trifluoroacetate catalyst as starting material. All values are quoted in kcal mol⁻¹. Bond distances are quoted in Å.

The addition of silver carbonate salt to intermediate **int-5b'** yielded structure **int-9b** that was highly stabilised. The carbonate anion first deprotonated the alcohol proton on pyridone ligand **L14**, without any barrier. The N-atom of the DG on the substrate got displaced as it got coordinated to the silver ion; this silver ion was also held in place by the deprotonated

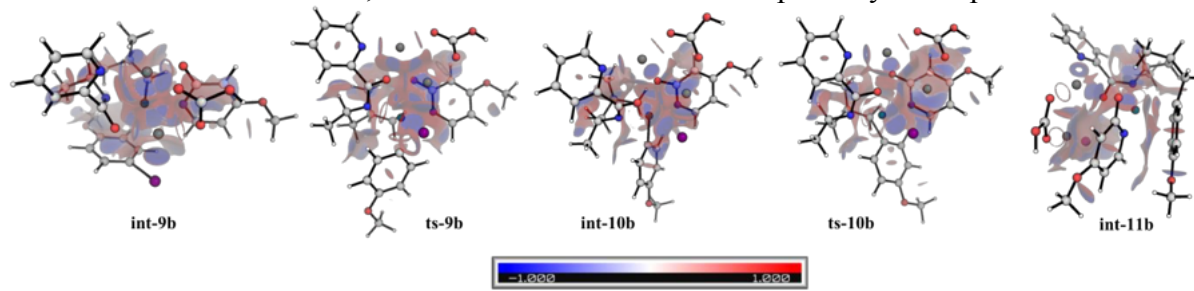


Figure S17. NCI plots of heterodimeric Pd-Ag catalytic structures at an isosurface value of 0.05 for second substrate in the presence of pyridone ligand **L2**.

alkoxy-oxygen on pyridone ligand **L14**. A second silver ion coordinated to two oxygen atoms and was held in close proximity to iodine, facilitating the formation of insoluble silver iodide salt as the reaction proceeded. These gave rise to stabilising non-covalent interactions (NCI) as can be seen in Figure S17 complex **int-9b**, showing attractive interactions between silver and iodine/oxygen atoms. In the highly organised transition structure **ts-9b**, NCIs existed to lower the

activation barrier (Figure S17), so that the OA barrier became 28.3 kcal mol⁻¹. With this, the C–H activation step, with a barrier of 31.0 kcal mol⁻¹, was overall rate-determining. We note that the pyridone ligand was necessary as the deprotonated alkoxy-oxygen played a crucial role in giving a highly ordered transition structure; replacing it with pyridine ligand results in the loss of this organisation, indicating that this could be a plausible reason why pyridine ligand did not work very well experimentally. For the second C–H activation, the TS **ts-11b'** occurs at a very high energy barrier relative to the first arylation product **int-11b**, which was highly stabilised. The activation barrier of 60.6 kcal mol⁻¹ was insurmountable such that the second arylation for this system was not observed, in agreement with experimental findings. To see if silver carbonate had any similar effect on the parent substrate **2a** in the presence of pyridine ligand **L1**, we performed a similar transition state search on the parent system in the presence of silver carbonate. Most TS searches failed to yield the expected structures due to the increased degree of freedom in the silver carbonate positions as pyridine could not hold silver ion in position after its N atom coordinates to Pd metal. The TS we found, **ts-9c** (at 11.0 kcal mol⁻¹), is higher in activation barrier than **ts-6** (at 7.1 kcal mol⁻¹) without the involvement of either pyridine or silver carbonate (Figure S18). NCI analysis (Figure S19) suggests that, in **ts-9c**, the pyridine ligand could not hold silver ion in a highly organised fashion as shown in **ts-9b** (Figure S17), therefore, the poorer interactions resulted in higher activation barriers.

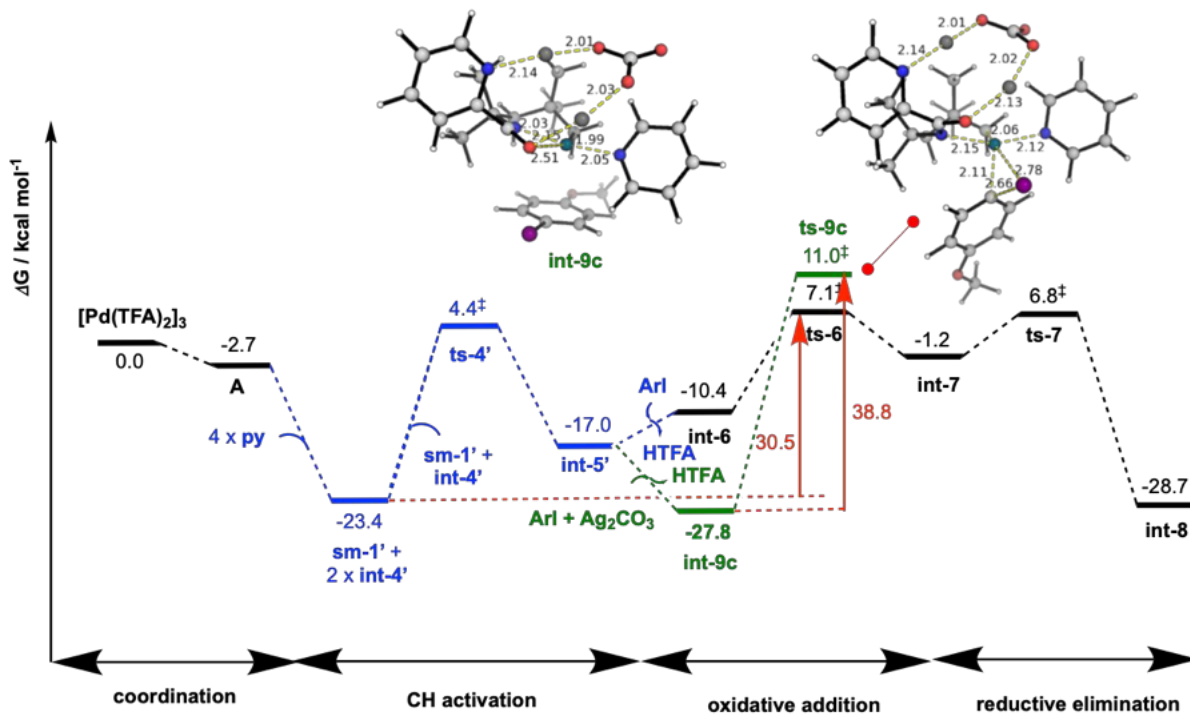


Figure S18. Computed Gibbs free energy profile for first arylation of parent substrate **1** in the presence of pyridine ligand **L1** and with (green) or without (black) silver carbonate with trimeric palladium trifluoroacetate catalyst as starting material. All values are quoted in kcal mol⁻¹.

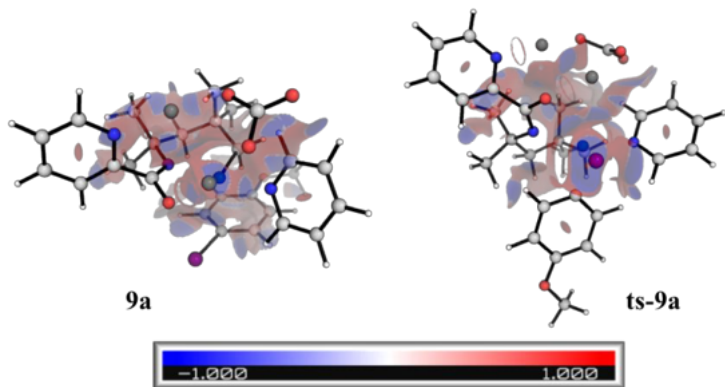


Figure S19. NCI plots of heterodimeric Pd-Ag catalytic structures for oxidative addition step at an isosurface value of 0.05 for parent substrate **1** in the presence of pyridine ligand **L1**.

III.4 C–H activation step

The different possibilities for the C–H activation step were considered (Figure S20) and lowest conformers were taken for discussion for earlier sections. Without pyridone ligand, the C–H activation step would be 3.4 kcal mol⁻¹ higher in activation barrier (**ts-4b**). Using pyridine in place of pyridone ligand, the C–H activation step would be 3.1–5.1 kcal mol⁻¹ higher depending on whether pyridine acts as a ligand (**ts-4b'-py**) or as a base (**ts-4b''-py**). In all cases, these were not as efficient as using pyridone ligand. The absence of Thorpe-Ingold effect in substrate **3a** renders the CMD r.d.s step more difficult. Using pyridine in addition to a separate TFA ion as a base were not as good in bringing the C–H bond into position for activation as using pyridone ligand as it can bring the C–H bond close to Pd(II) metal by N-coordination to the metal while carrying out the CMD step.

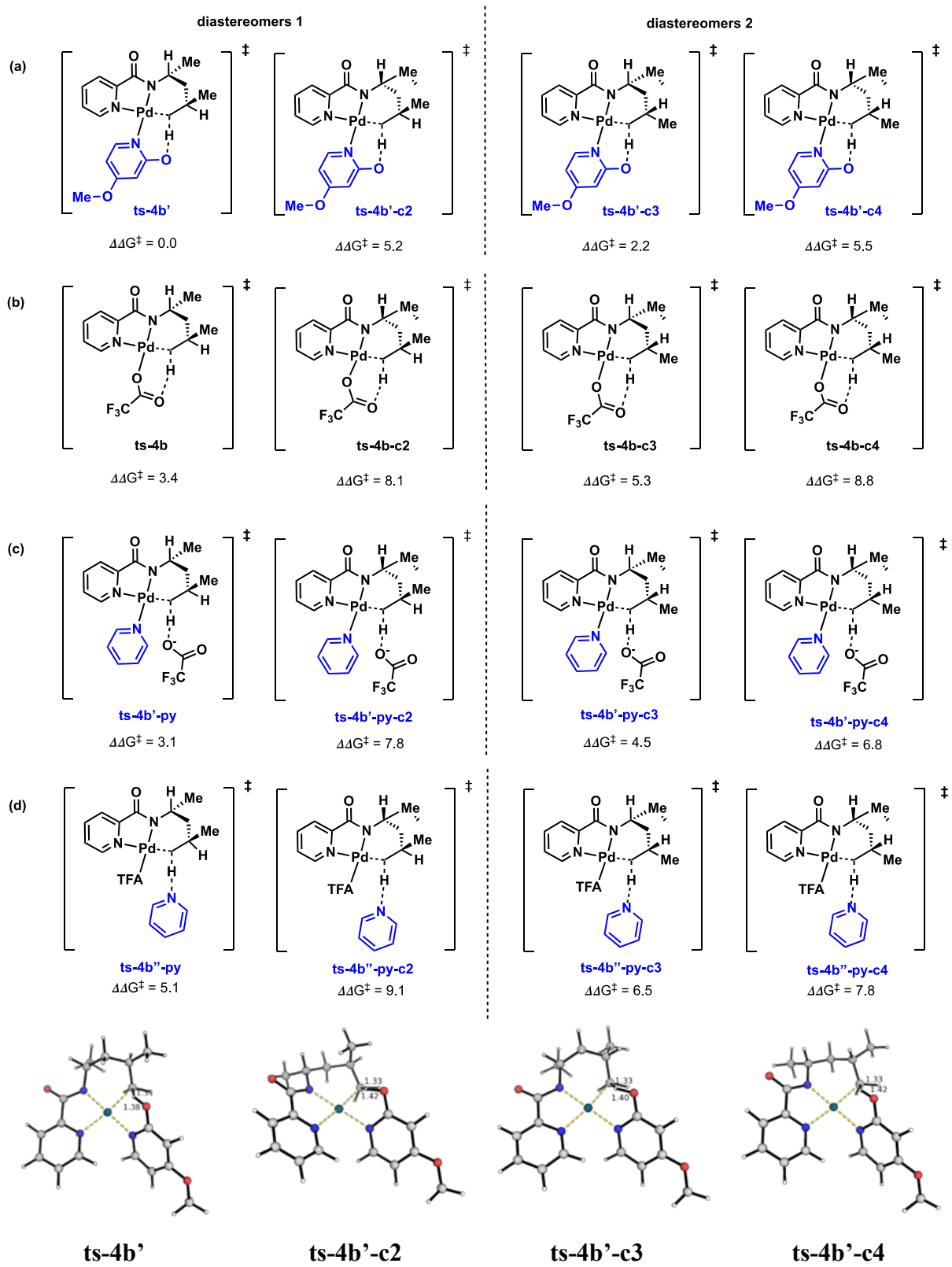


Figure S20. Different conformations considered for C–H activation step using (a) pyridone (b) TFA ion (c) TFA ion with pyridine as ligand (d) pyridine for the CMD step. All $\Delta\Delta G^\ddagger$ values are relative to the lowest activation barrier and are quoted in kcal mol⁻¹.

Importantly, our calculations gave the differences in the activation barrier $\Delta\Delta G^\ddagger$ between the two diastereomers (Figure S20 **ts-4b'** and **ts-4b'-c3**) as 2.2 kcal mol⁻¹. This corresponds to a diastereoselectivity of 21:1, in good agreement with experimentally observed ratio of 28:1. While the absolute configurations for the experimentally observed *d.r.* cannot be determined, computation allows us to establish the absolute stereochemistry of the arylated product with confidence.

III.5 Isodesmic formations of C–H activation step

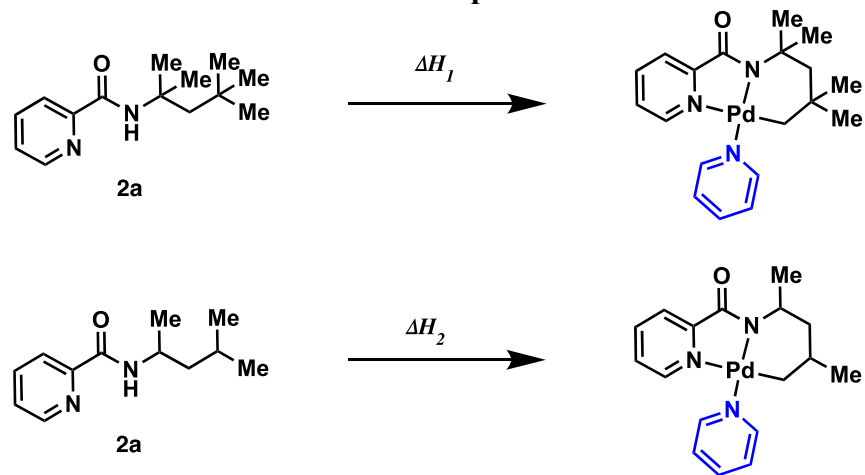


Figure S21. Isodesmic formations of pyridine-coordinated C–H activated complexes.

We consider the isodesmic reaction shown in Figure S21. Conformations of the products where the 6-membered rings buckled in different orientations were considered. For the second reaction, these include the products formed in Figure S20 (c) after losing an HTFA molecule. The lowest energy conformers for each reaction were used for comparison. The differences in the enthalpy, $\Delta\Delta H = \Delta H_1 - \Delta H_2$, gave the relative ease of formation of first C–H activated complex over the second one.

IV. Regioselectivity studies

IV.1 Regioselectivity in *N*-(4-methylhexan-2-yl)picolinamide (substrate 4a)

Substrate **4a** presented two inequivalent $\delta\text{-C}(sp^3)\text{-H}$ positions for arylation. To rationalise the observed regioselectivity, we calculated the relative energy differences ($\Delta\Delta G^\ddagger$) between the TSs for C–H activation step which was shown to be the r.d.s. for this reaction. The primary methyl C–H bond (**aa-1**) was selectively activated over secondary methylene C–H bond (two

conformations **4a-2-c1** and **4a-2-c2**); this was favoured by 2.3 kcal mol⁻¹, corresponding to a 24:1 selectivity for the primary C–H activation using simple transition state theory. NCI plots and van der Waals surfaces suggested that the unfavourable steric clashes between the ε -methyl group and the heterocyclic ring of **L14** and adjacent methyl groups account for the relative activation barriers observed experimentally (Figure S22). In TS **4a-2-c2**, there was only steric clashes between ε -methyl group and the heterocyclic ring of **L14**, whereas in TS **4a-2-c1**, in addition to the steric clashes between ε -methyl group and the heterocyclic ring of **L14**, there is additional steric clashes between ε -methyl group and the methyl group on α -carbon, such that TS **4a-2-c1** had higher activation barrier than TS **4a-2-c2**.

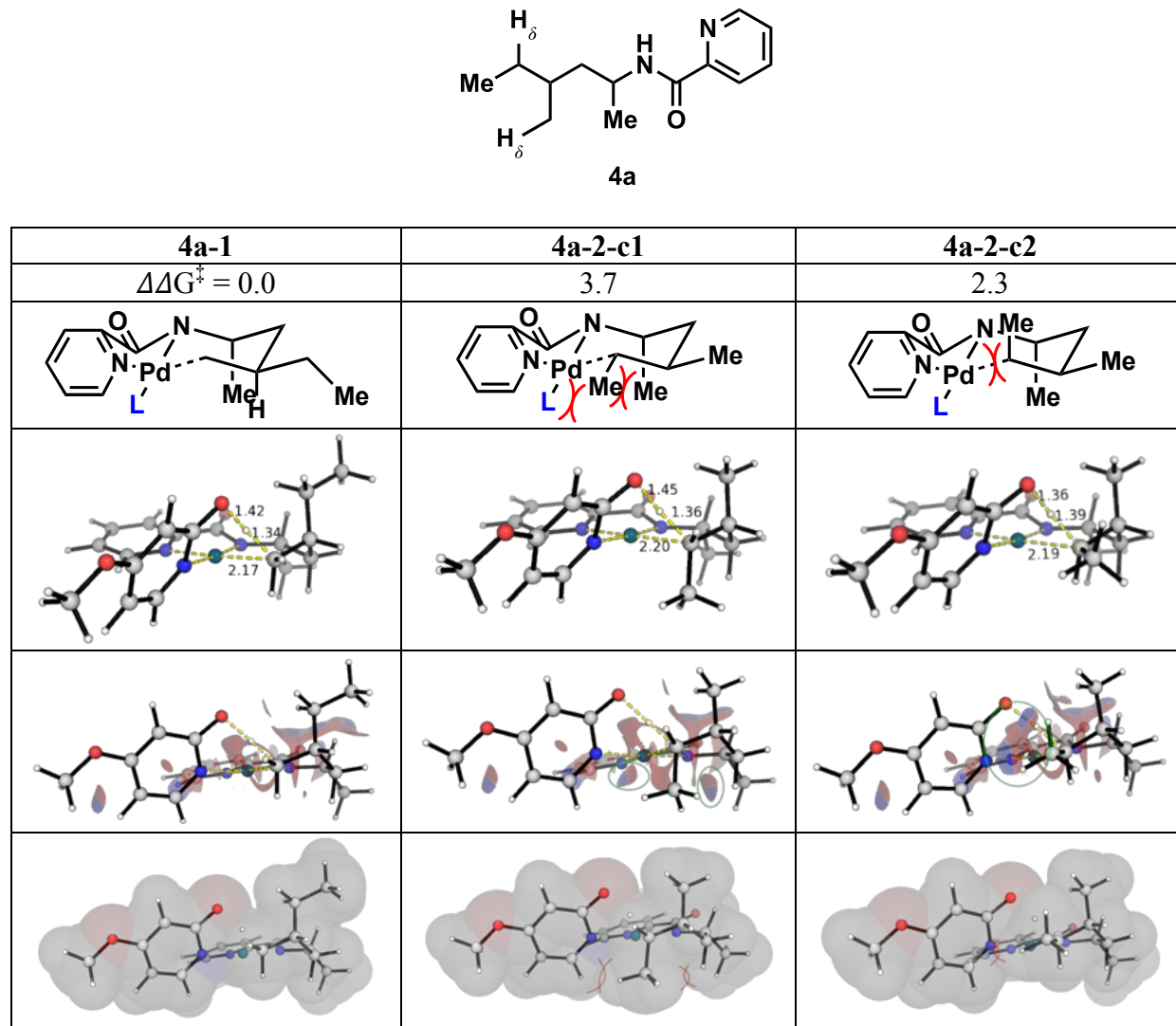
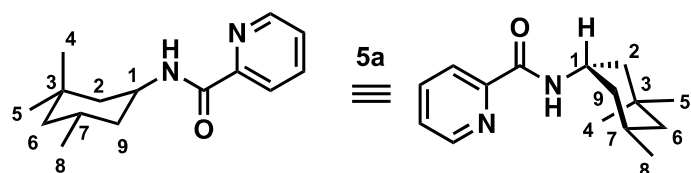
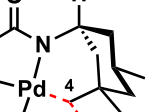
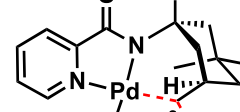
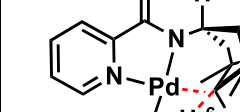
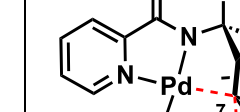
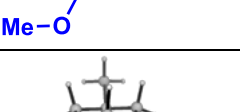
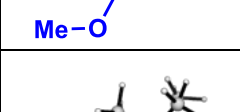
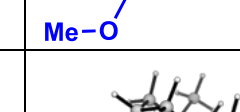


Figure S22. Optimised structures, NCI plots and van der Waals surfaces for C–H activation TSs of substrate **8a** by pyridone ligand **L14**. All $\Delta\Delta G^\ddagger$ values are quoted in kcal mol⁻¹. Bond distances are quoted in Å.

IV.2 Regioselectivity study in 3,5,5-trimethylcyclohexanamine (substrate 5a)

Substrate **5a** presented multiple inequivalent δ -C(sp^3)-H and γ -C(sp^3)-H positions for arylation. The relative energy differences ($\Delta\Delta G^\ddagger$) between the TSs were calculated. Four TSs were found for the C–H activation step (Figure S23). TS structure **5a-2** had a high activation barrier due to the distortion of the γ -H-atom while C–H activation occurred, giving rise to unfavourable interactions as shown in the NCI plots in Figure S23. Similarly, TS structures **5a-3** and **5a-4** distorted unfavourably, giving rise to elevated activation barriers. These were not competitive to TS **5a-1** that gave observed product. TS structures **5a-5** and **5a-6** were not computationally found (Figure S24); the activation of these C–H bonds would require placing a Me–H-group inside the palladacycle ring, giving rise to immensely repulsive interactions and were thus not observed experimentally.



5a-1	5a-2	5a-3	5a-4
$\Delta\Delta G^\ddagger = 0.0$	34.9	10.8	10.3
			
			

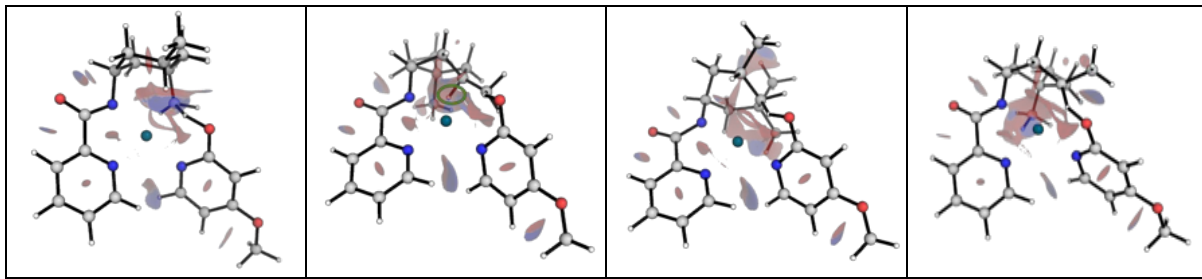


Figure S23. Optimised structures and NCI plots for C–H activation TSs of substrate **5a** by pyridone ligand **L14**. All $\Delta\Delta G^\ddagger$ values are quoted in kcal mol⁻¹. Bond distances are quoted in Å.

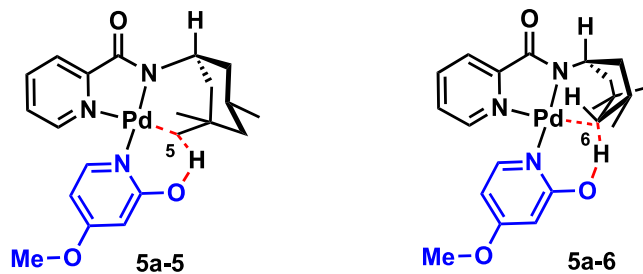
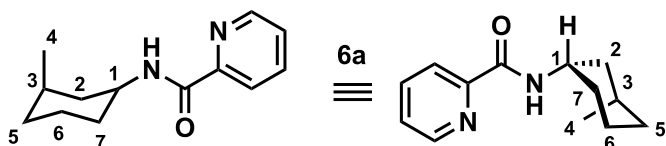


Figure S24. These TSs were impossible due to placing a Me-/H-group inside the palladacycle and were thus not found computationally.

IV.3 Regioselectivity study in 3-methylcyclohexanamine (substrate **6a**)

Substrate **6a** is structurally similar to substrate **5a**. The activation at γ -C(*sp*³)-H position would give less steric crowding than before (**5a-4**), due to fewer methyl groups present. Therefore, we recalculated this possibility. The relative energy difference ($\Delta\Delta G^\ddagger$) between the TSs for C–H activation step at δ -C(*sp*³)-H and γ -C(*sp*³)-H positions was 4.2 kcal mol⁻¹, corresponding to a 337:1 selectivity for the δ -C(*sp*³)-H position. The selectivity is again traced to non-covalent interactions present in these TSs (NCI plots, Figure S25).



6a-1	6a-2
$\Delta\Delta G^\ddagger = 0.0$	4.2

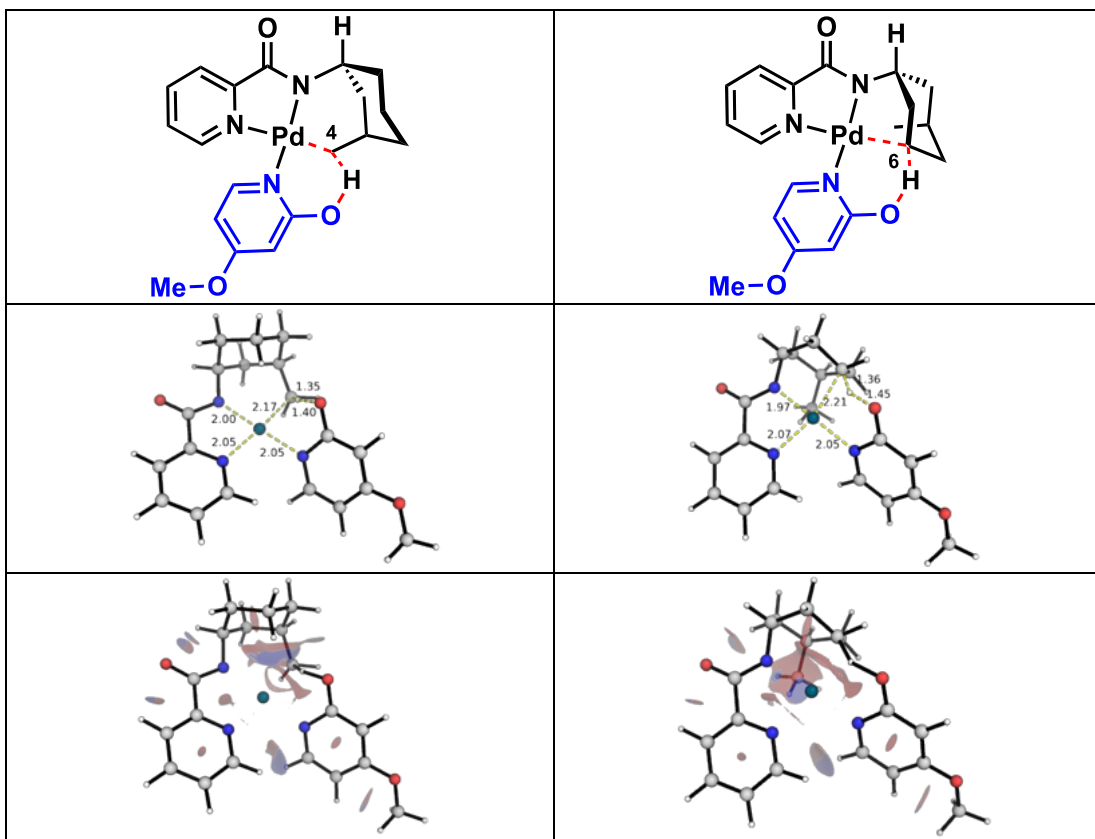
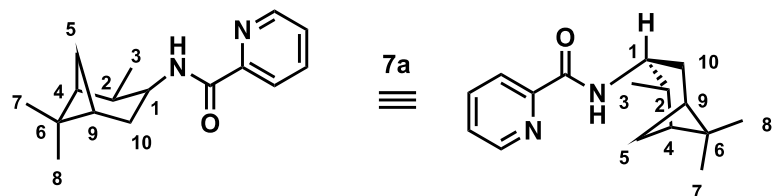


Figure S25. Optimised structures and NCI plots for regioselective C–H activation TSs of substrate **6a** by pyridone ligand **L14**. All $\Delta\Delta G^\ddagger$ values are quoted in kcal mol⁻¹. Bond distances are quoted in Å.

IV.4 Regioselectivity study in 3-pinanamine (substrate **7a**)

For substrate **7a**, we considered the regioselectivity between the secondary δ -C(sp^3)–H and the primary γ -C(sp^3)–H. Calculation predicted that the primary γ -C(sp^3)–H would be favoured by a factor of 56:1 over secondary δ -C(sp^3)–H provided that the C–H activation is the r.d.s. for this reaction ($\Delta\Delta G^\ddagger = 2.9$ kcal mol⁻¹ for γ -C(sp^3)–H activation). However, by including the oxidative insertion step, we found that oxidative insertion would be the r.d.s. for this reaction, with methylene δ -C(sp^3)–H functionalisation being 7.0 kcal mol⁻¹ lower than for γ -C(sp^3)–H activation, thus only methylene δ -C(sp^3)–H functionalisation was observed



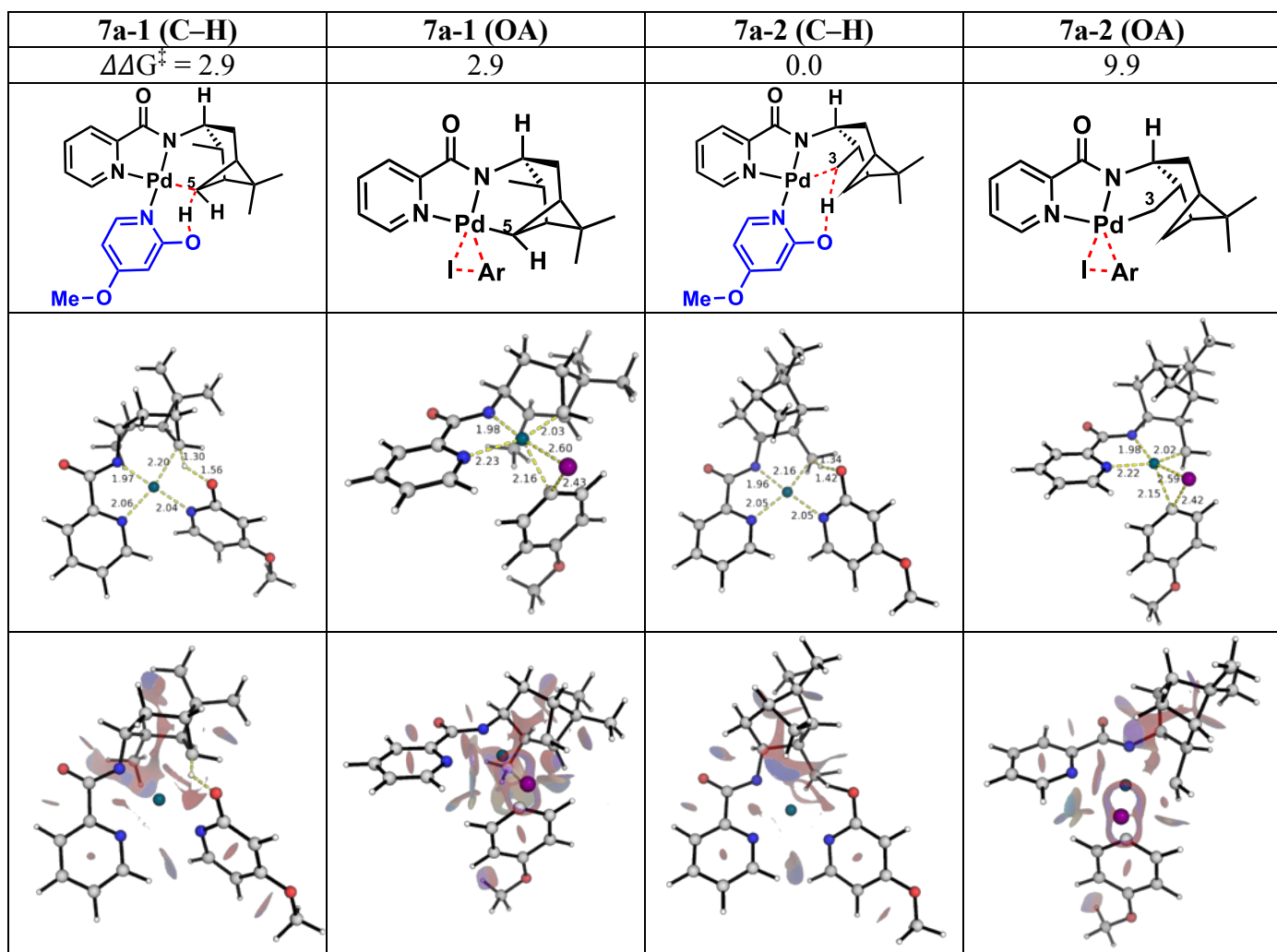
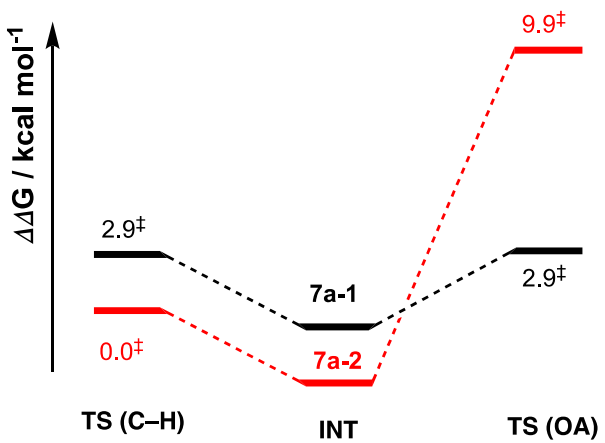


Figure S26. Optimised structures, NCI plots and van der Waals surfaces for C–H activation and oxidative insertion TSs of substrate **7a**. All $\Delta\Delta G^\ddagger$ values are taken relative to lowest TS energy and are quoted in kcal mol⁻¹. Bond distances are quoted in Å.

V. Absolute values for optimised structures

Structure	E/au	ZPE/au	H/au	qh-G/au	SP DFT (TBME)	Imaginary Freq/cm-1
Starting materials:						
1	-729.968887	0.341853	-729.60021	-729.679275	-730.885265	+
sm-1 - Pd(TFA)₂	-1178.318515	0.060493	-1178.2376	-1178.309077	-1179.642042	+
HTFA	-525.90441	0.04037	-525.85446	-525.89887	-526.575334	+
pyridine	-247.762761	0.089473	-247.66597	-247.704111	-248.071198	+
HI	-297.58318	0.005335	-297.57382	-297.599247	-297.586955	+
sm-1' - Pd(TFA)₂(py)₂	-1673.95914	0.244081	-1673.6783	-1673.782306	-1675.888255	+
[Pd(TFA)₂]₂	-2356.735982	0.123336	-2356.5716	-2356.686917	-2359.356276	+
[Pd(TFA)₂]₃	-3535.147025	0.186174	-3534.8983	-3535.058438	-3539.076728	+
ArI	-642.452756	0.123519	-642.31622	-642.369876	-642.880275	+
Ag₂CO₃	-556.727692	0.017256	-556.70052	-556.749839	-557.07963923	+
Pathway without pyridine ligand:						
A	-3943.294504	0.788308	-3942.4092	-3942.627445	-3947.711240	+
ts-A	-3943.241774	0.782901	-3942.3629	-3942.57849	-3947.652234	-1348.6927
B	-3943.251025	0.788085	-3942.3666	-3942.582852	-3947.664103	+
C	-3086.748426	0.466009	-3086.2138	-3086.379948	-3090.272882	+
int-1	-1908.345034	0.404572	-1907.8929	-1908.016055	-1910.578635	+
ts-1	-1908.32979	0.400691	-1907.8823	-1908.003846	-1910.556586	-197.3102
int-2	-1908.331012	0.403774	-1907.8796	-1908.002902	-1910.557829	+
int-3	-1382.415123	0.362564	-1382.0151	-1382.117512	-1383.984503	+
int-4	-1382.409747	0.361709	-1382.0106	-1382.112612	-1383.980311	+
ts-4	-1382.382482	0.357226	-1381.9887	-1382.088919	-1383.947170	-1413.066
int-5	-1382.397683	0.361725	-1381.9986	-1382.100732	-1383.964361	+
int-6	-1498.939203	0.444233	-1498.4533	-1498.564582	-1500.273756	+
ts-6	-1498.915736	0.444176	-1498.4309	-1498.539267	-1500.247698	-153.4792
int-7	-1498.929192	0.445017	-1498.4427	-1498.552903	-1500.260756	+
ts-7	-1498.917829	0.445413	-1498.4323	-1498.539302	-1500.250248	-264.4439

int-8	-1498.975689	0.446821	-1498.4881	-1498.597238	-1500.307462	+
int-9	-1727.288159	0.476923	-1726.7638	-1726.886036	-1729.280556	+
ts-9	-1727.260447	0.472307	-1726.7415	-1726.862309	-1729.246795	-1412.8
int-10	-1727.275647	0.476817	-1726.7514	-1726.874095	-1729.263882	+
int-11	-1843.817831	0.55929	-1843.2068	-1843.33841	-1845.574204	+
ts-11	-1843.794025	0.559109	-1843.1841	-1843.312942	-1845.547865	-154.7984
int-12	-1843.807344	0.56014	-1843.1957	-1843.326021	-1845.560782	+
ts-12	-1843.794662	0.560368	-1843.184	-1843.31127	-1845.548422	-264.5246
int-13	-1843.849056	0.561609	-1843.2366	-1843.36587	-1845.602114	+
int-14	-2072.15873	0.591842	-2071.5093	-2071.651746	-2074.571627	+
ts-14	-2072.133056	0.587093	-2071.4891	-2071.630185	-2074.539613	-1418.695
int-15	-2072.151155	0.591787	-2071.5017	-2071.644308	-2074.560538	+
int-16	-2188.698251	0.674641	-2187.9621	-2188.111875	-2190.872584	+
ts-16	-2188.671772	0.67382	-2187.9369	-2188.085877	-2190.846720	-161.358
int-17	-2188.691245	0.674902	-2187.9548	-2188.104679	-2190.865021	+
ts-17	-2188.670628	0.675537	-2187.9347	-2188.081475	-2190.844301	-269.7691
int-18	-2188.724769	0.676432	-2187.9873	-2188.136149	-2190.898783	+

Other TS conformers:

ts-4-c2	-1382.378401	0.357169	-1381.9847	-1382.084971	-1383.942824	-1463.7223
ts-6-c2	-1498.914551	0.444174	-1498.4298	-1498.537958	-1500.246335	
ts-7-c2	-1498.906846	0.445104	-1498.4213	-1498.529071	-1500.240529	-149.0566
ts-9-c2	-1727.252822	0.47248	-1726.7338	-1726.85426	-1729.238585	
ts-9-c3	-1727.238281	0.470924	-1726.7202	-1726.842025	-1729.225716	-275.7268
ts-9a	-1727.256169	0.472419	-1726.7372	-1726.857388	-1729.241314	-1468.4218
ts-9a-c2	-1727.256943	0.472254	-1726.738	-1726.858914	-1729.243140	-1337.0955
ts-9a-c3	-1727.236504	0.470877	-1726.7185	-1726.840138	-1729.223271	-1419.4
ts-11-c2	-1843.793136	0.559211	-1843.1833	-1843.311596	-1845.546678	-1466.6123
ts-11a	-1843.794362	0.559058	-1843.1846	-1843.31306	-1845.547631	-1335.1556
ts-11a-c2	-1843.792825	0.55918	-1843.183	-1843.311622	-1845.546357	-148.5601
ts-12-c2	-1843.784298	0.559999	-1843.1737	-1843.3	-1845.539637	-158.6799

ts-12a	-1843.79577	0.561431	-1843.1846	-1843.31018	-1845.546309	-148.9423
ts-12a-c2	-1843.786595	0.560107	-1843.176	-1843.3	-1845.541285	-266.8948
ts-14-c2	-2072.130558	0.587322	-2071.4865	-2071.627241	-2074.537572	-296.9839
ts-16-c2	-2188.668142	0.674459	-2187.933	-2188.080302	-2190.840673	-266.7996
ts-17-c2	-2188.66291	0.675125	-2187.9271	-2188.075084	-2190.838728	-1471.6767
ts-17-c3	-2188.667674	0.675351	-2187.9319	-2188.078887	-2190.841007	-151.15600
ts-17-c4	-2188.667511	0.676001	-2187.9314	-2188.077331	-2190.838337	
ts-17-c5	-2188.654308	0.674779	-2187.9189	-2188.066452	-2190.827057	-249.9004

Pathway with pyridine ligand:

int-4'	-1630.213178	0.453666	-1629.7138	-1629.832339	-1632.088801	-267.5227
ts-4'	-1630.16591	0.44849	-1629.6728	-1629.78823	-1632.041331	-270.3462
int-5'	-1104.271549	0.411573	-1103.8248	-1103.921267	-1105.4847000	+
ts-7'	-1746.69394	0.535902	-1746.1093	-1746.233232	-1748.325651	+
int-8'	-1746.788786	0.539053	-1746.2008	-1746.326492	-1748.425989	-1356.9381
int-9'	-1746.769913	0.538018	-1746.183	-1746.308063	-1748.403670	+
ts-9'	-1746.735932	0.533093	-1746.1545	-1746.278767	-1748.370295	-310.4541
int-10'	-1746.760532	0.538491	-1746.1733	-1746.298603	-1748.401135	+
int-13'	-2091.665624	0.655007	-2090.9523	-2091.094846	-2093.720383	+
int-14'	-2091.65048	0.652851	-2090.9385	-2091.083642	-2093.704809	-1403.9536
ts-14'	-2091.613357	0.647966	-2090.9069	-2091.051203	-2093.669270	+
int-15'	-2091.63819	0.653381	-2090.9259	-2091.071625	-2093.700360	+
int-19'	-2436.546862	0.76966	-2435.7084	-2435.872275	-2439.023104	+

Pathway with silver carbonate:

int-9c	-2303.536004	0.554597	-2302.9208	-2303.070999	-2305.506123	+
ts-9c	-2303.479916	0.554941	-2302.8658	-2303.011907	-2305.447408	+

Table S4. Absolute values (in Hartrees) for SCF energy, zero-point vibrational energy (ZPE), enthalpy and quasi-harmonic Gibbs free energy (at 363K) for the substrate **2a**. For harmonic frequency analysis, a plus (+) sign indicates that the lowest frequency of the optimised structures is positive, as expected.

Structure	E/au	ZPE/au	H/au	qh-G/au	SP DFT	Imaginary
-----------	------	--------	------	---------	--------	-----------

					(TBME)	Freq/cm-1
Starting materials:						
1b	-651.521636	0.286607	-651.21192	-651.284798	-652.33686421	+
L2	-437.183553	0.127404	-437.044	-437.093431	-437.73370834	+
sm-1' - Pd(TFA)₂(L2)₂	-2052.81663	0.318364	-2052.452	-2052.57549	-2055.22010719	+
Pathway without pyridone ligand:						
Ab	-3786.403409	0.678759	-3785.6354	-3785.841145	-3790.61949042	+
ts-Ab	-3786.350209	0.672608	-3785.5894	-3785.791664	-3790.56295244	-1373.5267
Bb	-3786.362329	0.677682	-3785.5961	-3785.79873	-3790.57732455	+
Cb	-3008.304508	0.410499	-3007.8291	-3007.988716	-3011.72978045	+
int-4b	-1303.971637	0.30689	-1303.6308	-1303.727538	-1305.44221842	+
ts-4b	-1303.928713	0.302166	-1303.594	-1303.687328	-1305.39328200	-1459.3829
int-5b	-1303.950556	0.306923	-1303.6105	-1303.704919	-1305.41703403	+
int-6b	-1420.491634	0.389299	-1420.0648	-1420.169024	-1421.72632082	+
ts-6b	-1420.466462	0.389483	-1420.0405	-1420.141597	-1421.69778098	-150.8472
int-7b	-1420.485571	0.390235	-1420.0581	-1420.160541	-1421.71744848	+
ts-7b	-1420.466776	0.390487	-1420.0401	-1420.140476	-1421.70021210	-295.8827
int-8b	-1420.525028	0.391015	-1420.097	-1420.199983	-1421.75848694	+
Pathway with pyridone ligand:						
int-3b'	-1741.211636	0.436383	-1740.7289	-1740.849534	-1743.21981744	+
int-4b'	-1215.219402	0.393066	-1214.7901	-1214.889912	-1216.57283801	+
ts-4b'	-1215.206067	0.388551	-1214.7821	-1214.879772	-1216.55605398	-1204.9058
int-5b'	-1215.249222	0.393651	-1214.8194	-1214.919205	-1216.60046818	+
int-6b'	-1857.723834	0.518585	-1857.155	-1857.283552	-1859.49536392	+
ts-6b'	-1857.673982	0.517182	-1857.107	-1857.234398	-1859.44115352	-220.1806
int-7b'	-1857.709236	0.520382	-1857.1393	-1857.265658	-1859.47519397	+
ts-7b'	-1857.678623	0.518787	-1857.1103	-1857.237165	-1859.45089825	-274.963
int-8b'	-1857.738157	0.520384	-1857.168	-1857.295489	-1859.50887950	+

ts-9b'	-1560.084214	0.503317	-1559.5353	-1559.654055	-1561.85663961	-1194.2607
Pathway with silver carbonate:						
int-9b	-2414.55588	0.535778	-2413.9578	-2414.111833	-2416.64889907	+
ts-9b	-2414.512268	0.535216	-2413.9155	-2414.067976	-2416.60392944	-220.8506
int-10b	-2414.554457	0.538329	-2413.9547	-2414.106738	-2416.64786796	+
ts-10b	-2414.517406	0.537287	-2413.919	-2414.070585	-2416.61455369	-327.8454
int-11b	-2414.581944	0.539712	-2413.9809	-2414.133427	-2416.67648220	+
Cationic pathways with silver carbonate and ligand:						
Na⁺ rct	-2019.759079	0.519972	-2019.1863	-2019.320319	-2021.62996259	+
Na⁺ ts	-2019.692981	0.518841	-2019.1219	-2019.254262	-2021.56731297	-224.7822
Ag⁺ rct	-2004.240092	0.517671	-2003.6685	-2003.806151	-2006.01162872	+
Ag⁺ ts	-2004.211399	0.517934	-2003.641	-2003.77383	-2005.98320200	-147.7256
C–H activation TSs						
ts-4b'	-1215.216342	0.389049	-1214.7921	-1214.889196	-1216.56560028	-1274.8426
ts-4b'-c2	-1215.209311	0.389145	-1214.785	-1214.881908	-1216.55767352	-1202.7765
ts-4b'-c3	-1215.213267	0.389383	-1214.7887	-1214.885752	-1216.56260083	-1159.6763
ts-4b'-c4	-1215.206067	0.388551	-1214.7821	-1214.879772	-1216.55605398	-1204.9058
ts-4b	-1303.935607	0.302195	-1303.6008	-1303.694079	-1305.40090816	-1403.0514
ts-4b-c2	-1303.928713	0.302166	-1303.594	-1303.687328	-1305.39328200	-1459.3829
ts-4b-c3	-1303.932987	0.302483	-1303.598	-1303.691129	-1305.39819713	-1391.205
ts-4b-c4	-1303.925561	0.301735	-1303.5911	-1303.684798	-1305.39148299	-1454.0579
ts-4b'-py	-1551.721357	0.393329	-1551.2873	-1551.395944	-1553.49772055	-1074.4733
ts-4b'-py-c2	-1551.714436	0.393545	-1551.2804	-1551.388666	-1553.49059485	-907.8496
ts-4b'-py-c3	-1551.718593	0.39359	-1551.2843	-1551.392981	-1553.49565720	-928.9741
ts-4b'-py-c4	-1551.712733	0.393009	-1551.2788	-1551.388023	-1553.49122815	-729.0941
ts-4b''-py	-1551.720548	0.392608	-1551.287	-1551.396477	-1553.49321197	-1358.2501
ts-4b''-py-c2	-1551.716725	0.392967	-1551.2831	-1551.391793	-1553.48772247	-1371.6569
ts-4b''-py-c3	-1551.71868	0.392871	-1551.2849	-1551.394333	-1553.49132619	-1317.4028
ts-4b''-py-c4	-1551.715779	0.392011	-1551.2826	-1551.392864	-1553.48773445	-1307.7334

Table S5. Absolute values (in Hartrees) for SCF energy, zero-point vibrational energy (ZPE), enthalpy and quasi-harmonic Gibbs free energy (at 363K) for substrate **3a**. For harmonic frequency analysis, a plus (+) sign indicates that the lowest frequency of the optimised structures is positive, as expected.

Structure	E/au	ZPE/au	H/au	qh-G/au	SP DFT (TBME)	Imaginary Freq/cm ⁻¹
Regioselectivity study of substrate 4a						
4a-1	-1254.435262	0.417625	-1253.9806	-1254.081325	-1255.83322982	-1211.2001
4a-2-c1	-1254.429616	0.417526	-1253.9749	-1254.075648	-1255.82736203	-1207.274
4a-2-c2	-1254.432952	0.417831	-1253.9781	-1254.078471	-1255.83003608	-1402.362
Regioselectivity study of substrate 5a						
5a-1	-1331.711312	0.45341	-1331.2193	-1331.322343	-1333.20195926	-1242.3319
5a-2	-1331.655993	0.45387	-1331.1635	-1331.266705	-1333.14909231	-1435.667
5a-3	-1331.693185	0.453096	-1331.201	-1331.30516	-1333.18496260	-1164.3307
5a-4	-1331.693357	0.452364	-1331.2019	-1331.305871	-1333.18486761	-1413.2075
Regioselectivity study of substrate 6a						
6a-1	-1253.255431	0.398722	-1252.8225	-1252.917322	-1254.64525533	-1252.1656
6a-2	-1253.245734	0.397452	-1252.8133	-1252.909895	-1254.63635977	-1141.9363
Regioselectivity study of substrate 7a						
7a-1 (C-H)	-1369.701419	0.459961	-1369.2022	-1369.306684	-1371.23536456	-704.7933
7a-1 (OA)						
7a-2 (C-H)	-1369.706545	0.459753	-1369.2078	-1369.311749	-1371.24003927	-1144.4993
7a-2	-1369.706545	0.459753	-1369.2078	-1369.311749	-1371.24003927	-1144.4993

Table S6. Absolute values (in Hartrees) for SCF energy, zero-point vibrational energy (ZPE), enthalpy and quasi-harmonic Gibbs free energy (at 363K) for regioselective TSs for C–H activation of substrate **4a**, **5a**, **6a** and **7a**.

VI. References:

Full reference for ref (1):

Gaussian 16, Revision A.01, Frisch, M. J.; Trucks, G. W.; Schlegel, H. B.; Scuseria, G. E.; Robb, M. A.; Cheeseman, J. R.; Scalmani, G.; Barone, V.; Mennucci, B.; Petersson, G. A.; Nakatsuji, H.; Caricato, M.; Li, X.; Hratchian, H. P.; Izmaylov, A. F.; Bloino, J.; Zheng, G.; Sonnenberg, J. L.; Hada, M.; Ehara, M.; Toyota, K.; Fukuda, R.; Hasegawa, J.; Ishida, M.; Nakajima, T.; Honda, Y.; Kitao, O.; Nakai, H.; Vreven, T.; Montgomery Jr., J. A.; Peralta, J. E.; Ogliaro, F.; Bearpark, M.; Heyd, J. J.; Brothers, E.; Kudin, K. N.; Staroverov, V. N.; Kobayashi, R.; Normand, J.; Raghavachari, K.; Rendell, A.; Burant, J. C.; Iyengar, S. S.; Tomasi, J.; Cossi, M.; Rega, N.; Millam, J. M.; Klene, M.; Knox, J. E.; Cross, J. B.; Bakken, V.; Adamo, C.; Jaramillo, J.; Gomperts, R.; Stratmann, R. E.; Yazyev, O.; Austin, A. J.; Cammi, R.; Pomelli, C.; Ochterski, J. W.; Martin, R. L.; Morokuma, K.; Zakrzewski, V. G.; Voth, G. A.; Salvador, P.; Dannenberg, J. J.; Dapprich, S.; Daniels, A. D.; Farkas, Ö.; Foresman, J. B.; Ortiz, J. V.; Cioslowski, J.; Fox, D. J. Gaussian, Inc., Wallingford CT, 2016.

- (1) Frisch, M. J.; Trucks, G. W.; Schlegel, H. B.; Scuseria, G. E.; Robb, M. A.; Cheeseman, J. R.; Scalmani, G.; Barone, V.; Mennucci, B.; Petersson, G. A.; et al. Gaussian 16, Revision A.01. 2016.
- (2) Yu, H. S.; He, X.; Li, S. L.; Truhlar, D. G. MN15: A Kohn–Sham Global-Hybrid Exchange–Correlation Density Functional with Broad Accuracy for Multi-Reference and Single-Reference Systems and Noncovalent Interactions. *Chem. Sci.* **2016**, *7* (8), 5032–5051. <https://doi.org/10.1039/C6SC00705H>.
- (3) Andrae, D.; Häußermann, U.; Dolg, M.; Stoll, H.; Preuß, H. Energy-Adjustedab Initio Pseudopotentials for the Second and Third Row Transition Elements. *Theor. Chim. Acta* **1990**, *77* (2), 123–141. <https://doi.org/10.1007/BF01114537>.
- (4) Rappoport, D.; Furche, F. Property-Optimized Gaussian Basis Sets for Molecular Response Calculations. *J. Chem. Phys.* **2010**, *133* (13), 134105. <https://doi.org/10.1063/1.3484283>.
- (5) Peterson, K. A.; Figgen, D.; Goll, E.; Stoll, H.; Dolg, M. Systematically Convergent Basis Sets with Relativistic Pseudopotentials. II. Small-Core Pseudopotentials and Correlation Consistent Basis Sets for the Post-d Group 16–18 Elements. *J. Chem. Phys.* **2003**, *119* (21), 11113–11123. <https://doi.org/10.1063/1.1622924>.
- (6) Weigend, F.; Ahlrichs, R. Balanced Basis Sets of Split Valence, Triple Zeta Valence and Quadruple Zeta Valence Quality for H to Rn: Design and Assessment of Accuracy. *Phys. Chem. Chem. Phys.* **2005**, *7* (18), 3297–3305. <https://doi.org/10.1039/B508541A>.
- (7) Weigend, F. Accurate Coulomb-Fitting Basis Sets for H to Rn. *Phys. Chem. Chem. Phys.* **2006**, *8* (9), 1057–1065. <https://doi.org/10.1039/B515623H>.
- (8) Mekareeya, A.; Walker, P. R.; Couce-Rios, A.; Campbell, C. D.; Steven, A.; Paton, R. S.; Anderson, E. A.; Ross Walker, P.; Couce-Rios, A.; Campbell, C. D.; et al. Mechanistic Insight into Palladium-Catalyzed Cycloisomerization: A Combined Experimental and Theoretical Study. *J. Am. Chem. Soc.* **2017**, *139* (29), 10104–10114. <https://doi.org/10.1021/jacs.7b05436>.
- (9) Deb, A.; Hazra, A.; Peng, Q.; Paton, R. S.; Maiti, D. Detailed Mechanistic Studies on

- Palladium-Catalyzed Selective C–H Olefination with Aliphatic Alkenes: A Significant Influence of Proton Shuttling. *J. Am. Chem. Soc.* **2017**, *139* (2), 763–775. <https://doi.org/10.1021/jacs.6b10309>.
- (10) Dandu, N. K.; Reed, J. A.; Odoh, S. O. Performance of Density Functional Theory for Predicting Methane-to-Methanol Conversion by a Tri-Copper Complex. *J. Phys. Chem. C* **2018**, *122* (2), 1024–1036. <https://doi.org/10.1021/acs.jpcc.7b09284>.
- (11) Marenich, A. V; Cramer, C. J.; Truhlar, D. G. Universal Solvation Model Based on Solute Electron Density and on a Continuum Model of the Solvent Defined by the Bulk Dielectric Constant and Atomic Surface Tensions. *J. Phys. Chem. B* **2009**, *113* (18), 6378–6396. <https://doi.org/10.1021/jp810292n>.
- (12) Murov, S. Properties of Organic Solvents <http://murov.info/orgsolvents.htm> (accessed May 3, 2018). <http://murov.info/orgsolvents.htm>.
- (13) Haynes, W. M.; Lide, D. R.; Bruno, T. J. CRC Handbook 97 Ed. In *CRC handbook of chemistry and physics: a ready-reference book of chemical and physical data.*; Raton, B., Ed.; Florida: CRC Press., 2016; pp 3–364.
- (14) Ulrich, N.; Endo, S.; Brown, T. N.; Watanabe, N.; Bronner, G.; Abraham, M. H.; Goss, K.-U. UFZ-LSER database v3.2.1 <http://www.ufz.de/lserd> (accessed Apr 30, 2018).
- (15) Wang, X.; Pan, J.; Wu, J.; Liu, Z. Surface Tension of Dimethoxymethane and Methyl Tert-Butyl Ether. *J. Chem. Eng. Data* **2006**, *51* (4), 1394–1397. <https://doi.org/10.1021/je060097q>.
- (16) Grimme, S. Supramolecular Binding Thermodynamics by Dispersion-Corrected Density Functional Theory. *Chem. – A Eur. J.* **2012**, *18* (32), 9955–9964. <https://doi.org/10.1002/chem.201200497>.
- (17) Funes-Ardoiz, I.; Paton, R. S. GoodVibes v1.0.1 <http://doi.org/10.5281/zenodo.56091>. <https://doi.org/10.5281/zenodo.56091>.
- (18) E. D. Glendening, A. E. Reed, J. E. Carpenter, and F. W. NBO Version 3.1.
- (19) Contreras-García, J.; Johnson, E. R.; Keinan, S.; Chaudret, R.; Piquemal, J.-P.; Beratan, D. N.; Yang, W. NCIPLOT: A Program for Plotting Noncovalent Interaction Regions. *J. Chem. Theory Comput.* **2011**, *7* (3), 625–632. <https://doi.org/10.1021/ct100641a>.
- (20) Sosa, C.; Andzelm, J.; Elkin, B. C.; Wimmer, E.; Dobbs, K. D.; Dixon, D. A. A Local Density Functional Study of the Structure and Vibrational Frequencies of Molecular Transition-Metal Compounds. *J. Phys. Chem.* **1992**, *96* (16), 6630–6636. <https://doi.org/10.1021/j100195a022>.
- (21) Godbout, N.; Salahub, D. R.; Andzelm, J.; Wimmer, E. Optimization of Gaussian-Type Basis Sets for Local Spin Density Functional Calculations. Part I. Boron through Neon, Optimization Technique and Validation. *Can. J. Chem.* **1992**, *70* (2), 560–571. <https://doi.org/10.1139/v92-079>.
- (22) Schrödinger, LLC. *The {PyMOL} Molecular Graphics Development Component, Version~1.8*; 2015.
- (23) Crumpton-Bregel, D. M.; Goldberg, K. I.; and, D. M. C.-B.; Goldberg, K. I. Mechanisms of C–C and C–H Alkane Reductive Eliminations from Octahedral Pt(IV): Reaction via Five-Coordinate Intermediates or Direct Elimination? *J. Am. Chem. Soc.* **2003**, *125* (31), 9442–9456. <https://doi.org/10.1021/ja029140u>.
- (24) Skapski, A. C.; Smart, M. L. The Crystal Structure of Trimeric Palladium(II) Acetate. *J. Chem. Soc. D* **1970**, *11*, 658b–659. <https://doi.org/10.1039/C2970000658B>.
- (25) Bakmutov, V. I.; Berry, J. F.; Cotton, F. A.; Ibragimov, S.; Murillo, C. A. Non-Trivial

- Behavior of Palladium(II) Acetate. *Dalt. Trans.* **2005**, *11*, 1989–1992.
<https://doi.org/10.1039/B502122G>.
- (26) Vana, J.; Hanusek, J.; Sedlak, M. Bi and Trinuclear Complexes in Palladium Carboxylate-Assisted C-H Activation Reactions. *Dalt. Trans.* **2018**, *47* (5), 1378–1382.
<https://doi.org/10.1039/C7DT04269H>.
- (27) Diao, T.; White, P.; Guzei, I.; Stahl, S. S. Characterization of DMSO Coordination to Palladium(II) in Solution and Insights into the Aerobic Oxidation Catalyst, Pd(DMSO)2(TFA)2. *Inorg. Chem.* **2012**, *51* (21), 11898–11909.
<https://doi.org/10.1021/ic301799p>.
- (28) Sankaralingam, M.; Vadivelu, P.; Palaniandavar, M. Novel Nickel(II) Complexes of Sterically Modified Linear N4 Ligands: Effect of Ligand Stereoelectronic Factors and Solvent of Coordination on Nickel(II) Spin-State and Catalytic Alkane Hydroxylation. *Dalt. Trans.* **2017**, *46*. <https://doi.org/10.1039/c7dt00576h>.
- (29) Vana, J.; Lang, J.; Soltesova, M.; Hanusek, J.; Ruzicka, A.; Sedlak, M.; Roithova, J. The Role of Trinuclear Species in a Palladium Acetate/Trifluoroacetic Acid Catalytic System. *Dalt. Trans.* **2017**, *46* (46), 16269–16275. <https://doi.org/10.1039/C7DT03832A>.
- (30) Haines, B. E.; Berry, J. F.; Yu, J.-Q.; Musaev, D. G. Factors Controlling Stability and Reactivity of Dimeric Pd(II) Complexes in C–H Functionalization Catalysis. *ACS Catal.* **2016**, *6* (2), 829–839. <https://doi.org/10.1021/acscatal.5b02447>.
- (31) Giri, R.; Lan, Y.; Liu, P.; Houk, K. N.; Yu, J.-Q. Understanding Reactivity and Stereoselectivity in Palladium-Catalyzed Diastereoselective Sp^3 C–H Bond Activation: Intermediate Characterization and Computational Studies. *J. Am. Chem. Soc.* **2012**, *134* (34), 14118–14126. <https://doi.org/10.1021/ja304643e>.
- (32) Dang, Y.; Qu, S.; Nelson, J. W.; Pham, H. D.; Wang, Z. X.; Wang, X. The Mechanism of a Ligand-Promoted C(Sp^3)-H Activation and Arylation Reaction via Palladium Catalysis: Theoretical Demonstration of a Pd(II)/Pd(IV) Redox Manifold. *J. Am. Chem. Soc.* **2015**, *137* (5), 2006–2014. <https://doi.org/10.1021/ja512374g>.
- (33) Ano, Y.; Tobisu, M.; Chatani, N. Palladium-Catalyzed Direct Ethynylation of C(Sp^3)-H Bonds in Aliphatic Carboxylic Acid Derivatives. *J. Am. Chem. Soc.* **2011**, *133* (33), 12984–12986. <https://doi.org/10.1021/ja206002m>.
- (34) Cui, W.; Chen, S.; Wu, J. Q.; Zhao, X.; Hu, W.; Wang, H. Palladium-Catalyzed Remote C(Sp^3)-H Arylation of 3-Pinanamine. *Org. Lett.* **2014**, *16* (16), 4288–4291.
<https://doi.org/10.1021/o1502011k>.
- (35) He, G.; Zhang, S.-Y.; Nack, W. A.; Li, Q.; Chen, G. Use of a Readily Removable Auxiliary Group for the Synthesis of Pyrrolidones by the Palladium-Catalyzed Intramolecular Amination of Unactivated γ C(Sp^3)-H Bonds. *Angew. Chemie Int. Ed.* **2013**, *52* (42), 11124–11128. <https://doi.org/10.1002/anie.201305615>.
- (36) He, G.; Chen, G. A Practical Strategy for the Structural Diversification of Aliphatic Scaffolds through the Palladium-Catalyzed Picolinamide-Directed Remote Functionalization of Unactivated C(Sp^3)-H Bonds. *Angew. Chemie Int. Ed.* **2011**, *50* (22), 5192–5196. <https://doi.org/10.1002/anie.201100984>.
- (37) He, J.; Li, S.; Deng, Y.; Fu, H.; Laforteza, B. N.; Spangler, J. E.; Homs, A.; Yu, J.-Q. Ligand-Controlled C(Sp^3)-H Arylation and Olefination in Synthesis of Unnatural Chiral α -Amino Acids. *Science* **2014**, *343* (6176), 1216–1220.
<https://doi.org/10.1126/science.1249198>.
- (38) Li, S.; Zhu, R.-Y.; Xiao, K.-J.; Yu, J.-Q. Ligand-Enabled Arylation of γ -C–H Bonds.

Angew. Chemie Int. Ed. **2016**, *55* (13), 4317–4321.

<https://doi.org/10.1002/anie.201512020>.

- (39) Rodríguez, N.; Romero-Revilla, J. A.; Fernández-Ibáñez, M. Á.; Carretero, J. C. Palladium-Catalyzed N-(2-Pyridyl)Sulfonyl-Directed C(Sp₃)-H γ -Arylation of Amino Acid Derivatives. *Chem. Sci.* **2013**, *4* (1), 175–179. <https://doi.org/10.1039/c2sc21162a>.
- (40) O'Duill, M. L.; Matsuura, R.; Wang, Y.; Turnbull, J. L.; Gurak, J. A.; Gao, D. W.; Lu, G.; Liu, P.; Engle, K. M. Tridentate Directing Groups Stabilize 6-Membered Palladacycles in Catalytic Alkene Hydrofunctionalization. *J. Am. Chem. Soc.* **2017**, *139* (44), 15576–15579. <https://doi.org/10.1021/jacs.7b08383>.
- (41) Liu, Z.; Wang, Y.; Wang, Z.; Zeng, T.; Liu, P.; Engle, K. M. Catalytic Intermolecular Carboamination of Unactivated Alkenes via Directed Aminopalladation. *J. Am. Chem. Soc.* **2017**, *139* (32), 11261–11270. <https://doi.org/10.1021/jacs.7b06520>.
- (42) Proutiere, F.; Schoenebeck, F. Orthogonal Selectivities under Pd(0) Catalysis with Solvent Polarity: An Interplay of Computational and Experimental Studies. *Synlett* **2012**, *23* (05), 645–648. <https://doi.org/10.1055/s-0031-1290564>.
- (43) Plata, R. E.; Singleton, D. A. A Case Study of the Mechanism of Alcohol-Mediated Morita Baylis-Hillman Reactions. the Importance of Experimental Observations. *J. Am. Chem. Soc.* **2015**, *137* (11), 3811–3826. <https://doi.org/10.1021/ja5111392>.
- (44) Yang, Y. F.; Cheng, G. J.; Liu, P.; Leow, D.; Sun, T. Y.; Chen, P.; Zhang, X.; Yu, J. Q.; Wu, Y. D.; Houk, K. N. Palladium-Catalyzed Meta-Selective C–H Bond Activation with a Nitrile-Containing Template: Computational Study on Mechanism and Origins of Selectivity. *J. Am. Chem. Soc.* **2014**, *136* (1), 344–355. <https://doi.org/10.1021/ja410485g>.
- (45) Anand, M.; Sunoj, R. B.; Schaefer, H. F. Non-Innocent Additives in a Palladium(II)-Catalyzed C–H Bond Activation Reaction: Insights into Multimetallic Active Catalysts. *J. Am. Chem. Soc.* **2014**, *136* (15), 5535–5538. <https://doi.org/10.1021/ja412770h>.